

**PRELIMINARY INDIRECT MEASUREMENT OF
COSMIC-RAY PROTON SPECTRUM USING EARTH'S
 γ -RAY DATA FROM *FERMI* LARGE AREA TELESCOPE**

PATOMPORN PAYOUNGKHAMDEE

**A THESIS SUBMITTED IN PARTIAL FULFILLMENT
OF THE REQUIREMENTS FOR
THE DEGREE OF MASTER OF SCIENCE (PHYSICS)
FACULTY OF GRADUATE STUDIES
MAHIDOL UNIVERSITY
2021**

COPYRIGHT OF MAHIDOL UNIVERSITY

Thesis
entitled

.....
Mr. Patomporn Payoungkhamdee
Candidate

.....
Asst. Prof. Warit Mitthumsiri,
Ph.D. (Physics)
Major advisor

.....
Prof. David Ruffolo,
Ph.D. (Physics)
Co-advisor

.....
Dr. Alejandro Sáiz,
Ph.D. (Physics)
Co-advisor

.....
Prof. Patcharee Lertrit,
M.D., Ph.D. (Biochemistry)
Dean
Faculty of Graduate Studies
Mahidol University

.....
Assoc. Prof. Kittiwit Matan,
Ph.D. (Physics)
Program Director
Master of Science Program in Physics
(International Program)
Faculty of Science
Mahidol University

Thesis
entitled

was submitted to the Faculty of Graduate Studies, Mahidol University
for the degree of Master of Science (Physics)
on
May 18, 2020

.....
Mr. Patomporn Payoungkhamdee
Candidate

.....
Assoc. Prof. Paisan Tooprakai,
Ph.D. (Physics)
Chair

.....
Asst. Prof. Warit Mitthumsiri,
Ph.D. (Physics)
Member

.....
Prof. David Ruffolo,
Ph.D. (Physics)
Member

.....
Prof. Patcharee Lertrit,
M.D., Ph.D. (Biochemistry)
Dean
Faculty of Graduate Studies
Mahidol University

.....
Assoc. Prof. Palangpon Kongsaree,
Ph.D. (Organic Chemistry)
Dean
Faculty of Science
Mahidol University

ACKNOWLEDGEMENTS

Thanks to the members of space physics laboratory..

Patomporn Payoungkhamdee

PRELIMINARY INDIRECT MEASUREMENT OF COSMIC-RAY PROTON SPECTRUM USING EARTH'S γ -RAY DATA FROM *FERMI* LARGE AREA TELESCOPE.

PATOMPORN PAYOUNGKHAMDEE 5736149 SCPY/D

M.Sc. (PHYSICS)

THESIS ADVISORY COMMITTEE: WARIT MITTHUMSIRI, Ph.D. (PHYSICS), DAVID RUFFOLO, Ph.D. (PHYSICS), ALEJANDRO SÁIZ, Ph.D. (PHYSICS)

ABSTRACT

Cosmic rays (CRs) are high-energy particles, mostly protons, propagating in space. The rigidity (momentum per charge) spectrum of CRs is well described by a power law for which the spectral index is approximately 2.8 around 30 - 1000 GV. Recent measurements by PAMELA and AMS-02 indicate an abrupt change of the CR proton spectral index at about 340 GV. When CRs interact with the Earth's upper atmosphere, γ rays can be produced and detected by space-based detectors. Here we use the Earth's γ -ray data collected by the *Fermi* Large Area Telescope along with a proton-air interaction model to indirectly determine the CR proton spectral index and compare against observations by other instruments.

KEY WORDS: COSMIC RAYS / EARTH'S GAMMA RAYS

68 pages

CONTENTS

	Page
ACKNOWLEDGEMENTS	iii
ABSTRACT (ENGLISH)	iv
LIST OF TABLES	vii
LIST OF FIGURES	viii
CHAPTER I INTRODUCTION	1
1.1 Overview	1
1.2 Objectives	2
1.3 Outline of Thesis	3
CHAPTER II BACKGROUND	4
2.1 Cosmic Ray	4
2.1.1 History	4
2.1.2 Physical properties	7
2.1.3 γ -ray production	9
2.2 <i>Fermi</i> Large Area Telescope (LAT)	13
2.2.1 Overview	13
2.2.2 Large Area Telescope (LAT)	14
2.2.3 Event reconstruction	18
2.2.4 LAT performance and characteristics	18
CHAPTER III LITERATURE REVIEW	22
CHAPTER IV METHODOLOGY	30
4.1 Data selection	31
4.2 Flux extraction	31
4.2.1 Exposure map gathering	32
4.3 Hadronic Collision Model	38
4.4 Optimization	40

CONTENTS (cont.)

	Page
4.5 Statistical significance	42
CHAPTER V RESULTS AND DISCUSSION	44
5.1 Limb's angle correction	44
5.2 γ -ray spectrum measurement	45
5.3 Best fit result	51
CHAPTER VI CONCLUSION	54
REFERENCES	55
APPENDICES	63
Appendix A Testing the exposure map	64
Appendix B Power law in energy	65
Appendix C Subtracting γ -ray background	66
Appendix D Interaction Model	67
BIOGRAPHY	68

LIST OF TABLES

Table	Page
5.1 Optimization results	51

LIST OF FIGURES

Figure	Page
2.1 Wulf's apparatus and the balloon experimental results	4
2.2 (left) Clay's experiment on the geographical variation of CR intensity. Main locations where CR intensity was measured during 8 Compton's expeditions in 1932. (right) The Pb-shielded ionization chamber, organized by Compton. Image taken from Dorman (2009)	5
2.3 Latitude variation of CR intensity for various seasons (Compton & Turner 1937)	6
2.4 The CR spectrum showing the superposition of different populations of sources (Taylor 2016)	7
2.5 Simplified schematic of CR proton air shower (Image taken from Cosmic Rays, Wikipedia, Magnus Manske, 2011)	9
2.6 Feynman's diagram of the neutral pion (π^0) decay into two γ -rays.	10
2.7 Lepton-antilepton annihilation path diagram.	10
2.8 First-order Feynman's diagrams for the Compton and Inverse Compton processes.	11
2.9 Intensity of γ -ray > 1 GeV in galactic coordinates (Image credit: NASA/DOE/ <i>Fermi</i> LAT Collaboration).	12
2.10 Main components of the LAT and the GBM on the <i>Fermi</i> Space Telescope (Michelson et al. 2010)	13
2.11 Main components of the LAT (Image taken from https://fermi.gsfc.nasa.gov)	14
2.12 Schematic of γ -ray detection of the LAT (Image taken from https://fermi.gsfc.nasa.gov)	

2.13 LAT's particle tracker. (a) The ideal case where the conversion happen in an early layer and leave a footprint along multiple layers (b). (c) The photon skips first layer and be converted in another layer with a missed hit in 1st and 2nd of Si trackers (d). (e) Conversion occurs in structural materials and be traced by the following Si trackers. (Atwood et al. 2009)	16
2.14 LAT's calorimeter (Atwood et al. 2009)	17
2.15 Flow chart of LAT's data acquisition system (DAQ) (Image taken from Atwood et al. (2009))	17
2.16 Effective area along the photon energy range from MeV to TeV (Maldera 2019)	19
2.17 Effective area versus incidence angle (Maldera 2019)	19
2.18 LAT's effective area versus azimuthal angle for a 10 GeV photon with the incidence angle of 30° (Maldera 2019).	20
2.19 Effective area along the energy of each event class (Maldera 2019)	20
3.1 Cosmic-ray elemental spectra from various experiments (Beringer et al. 2012)	23
3.2 World map with computed geomagnetic vertical cutoff rigidity contour lines on a given date (B. et al. 2007)	24
3.3 The asymmetry of γ -rays East-West intensity	24
3.4 γ -ray intensity along the zenith angle (Kraushaar et al. 1965)	25
3.5 The Earth's centered intensity plot from the satellite based observations	
	26
3.6 Calculated γ -ray intensity with the variation of zenithal angle (Morris 1984)	26
3.7 γ -ray spectrum from proton-nuclei interactions (Morris 1984)	27
3.8 γ -rays intensity from limb emission in 4 energy ranges (Abdo et al. 2009)	28
4.1 Schematics of γ -ray production	30
4.2 Coordinate transform between celestial and spacecraft	33
4.3 Coordinate transform between spacecraft and nadir angle	34

4.4	Detector's boresight in cartesian and polar coordinate	36
4.5	Spawning the king and slave processes	37
4.6	Master process send a small task to workers	38
4.7	Aynchronous sending to an available worker	38
5.1	Distribution of nadir angle before and after altitude correction	44
5.2	An example distribution of γ -ray from a single week	45
5.3	Cartesian plot of the photon histograms (title represent mean of the energy range)	46
5.4	Polar plot of the photon histograms	47
5.5	Cartesian plot of the exposure histograms	48
5.6	Polar plot of the exposure histograms	49
5.7	Measured γ -ray spectrum	49
5.8	Cartesian plot of the flux histograms	50
5.9	Polar plot of the flux histograms	51
5.10	The γ -ray spectra calculated from the SPL (red) and BPL (blue) models of CR proton which best fit with the measured Earth's γ -ray spectrum in the thin-target regime (red)	52
5.11	Best-fit CR proton spectrum from this work (red) compared to the measurements by AMS-02 (blue) and PAMELA (green)	53

CHAPTER I

INTRODUCTION

1.1 Overview

Space is full of fascinating phenomena, why stars are bright to more advanced questions such as whether dark matter exists. Human curiosity has brought us so far that now we can observe the sky with more sophisticated techniques. However, the research to gather new knowledge by studying the space is endless. The answer to one question sometimes generate another mystery. Research in physical science also helps creating new technology because of the need to overcome challenging limitations of the instruments or techniques.

The frontier of astrophysical research is continually expanding over time because the exploration of one thing does open the new door to another dark room which has been waiting for human to shine a light to explore. There are various branches in astrophysics from theoretical foundation, simulation and experimental physics which all compliment each other for pushing the frontier of the human knowledge. To study high energy particle accelerators in the universe, the possibility of direct probing of multiple Galactic sources which produce high-energy particles, or cosmic rays (CRs), is nearly impossible in terms of current technology and resources required. Nevertheless, the technology of observing the particles arriving the Earth is more plausible for scientists.

CRs can be observed with two types of detectors: ground-based and spaced-based. Analyzing and studying CR data allows us to interpret properties of their sources and cosmic environment.

The spectrum of CRs follows a power law with different spectral indices depending on the rigidity (momentum per charge) range of particles. There are multiple types of CR sources in space including unknown sources. There are multiple types of CR sources in space including unknown sources. Consequently,

changing of the spectral index from one rigidity to another rigidity will find the discontinuity if there is the translation from one source type to another source from the superposition of multiple spectrums.

Fermi-LAT has been launched to orbit around the Earth and monitor the γ -ray sky. Interestingly, the brightest γ -ray source in the sky for the LAT is the Earth's limb due to its proximity. At above 1 GeV, the Earth's γ -ray emission from CRs interacting with the upper atmosphere appears as a bright ring (Abdo et al. 2009).

Before 2010, there were some hints of the abrupt change in the CR spectral index at 300 GV in rigidity by some experiments (Adriani et al. 2011; Seo et al. 2004; Isbert et al. 2002; Haino et al. 2004), though the conclusion was from the combination of data from different experiments which is prone to the systematic uncertainty. In 2014, Fermi LAT attempted to measure this spectral feature indirectly using the Earth's γ -ray emission data from 5 years of observations (Ackermann et al. 2014). The inferred spectral indices are consistent with other experiment, showing a spectral break at around 300 GV with $\approx 1\sigma$ significance level, which is not high enough to make a definitive conclusion.

1.2 Objectives

The objectives of this study are to

- To indirectly measure the CR proton spectrum between approximately 60 – 1000 GV in rigidity.
- To build on the results from the previous study with more dataset
- To improve the optimizaiton technique by using the heuristical methodology
- To reduce the calculation time by inventing a new parallel code in low level from scratch

1.3 Outline of Thesis

The dissertation provides various information from the overview introductory context to the technical detail employed in this study as well as the results and interpretations. It is structured as follows.

Chapter I provides the overview and objectives of this work.

Chapter II is the background knowledge relating to this study. This chapter also provides brief history of cosmic ray research which contains impactful experiments and important findings which have advanced the field. Some theoretical detail will be provided along with the historical discoveries. Subchapters describe in more detail about high-energy astroparticle physics.

Chapter III consists of multiple literature reviews involving the study to clarify the theoretical idea as well as for filling the concepts which are important for our better understanding of the next chapter.

Chapter IV consists of datasets selection, flux calculation , computation optimization and interpretation. The following chapter which is chapter V will be the discussion from the analyzed results. The last chapter

The last chapter (Chapter V) is the final summarization from this study. It composed of the final numerical results and the statistical significance.

CHAPTER II

BACKGROUND

2.1 Cosmic Ray

This section discusses the historical discoveries from early studies in the field to the latest high-impact experiments.

2.1.1 History

In 1909, Theodor Wolf conducted the famous experiment that pioneered the study of cosmic rays (CRs) by taking an apparatus to measure the rate of ionization from the ground to the top of the Eiffel Tower in Paris (Gray 1949). The result showed that the ionization rate was slightly increased with the altitude is higher which provided a clue that the origin of CRs was from outer space rather than from the Earth (Hörandel 2013).

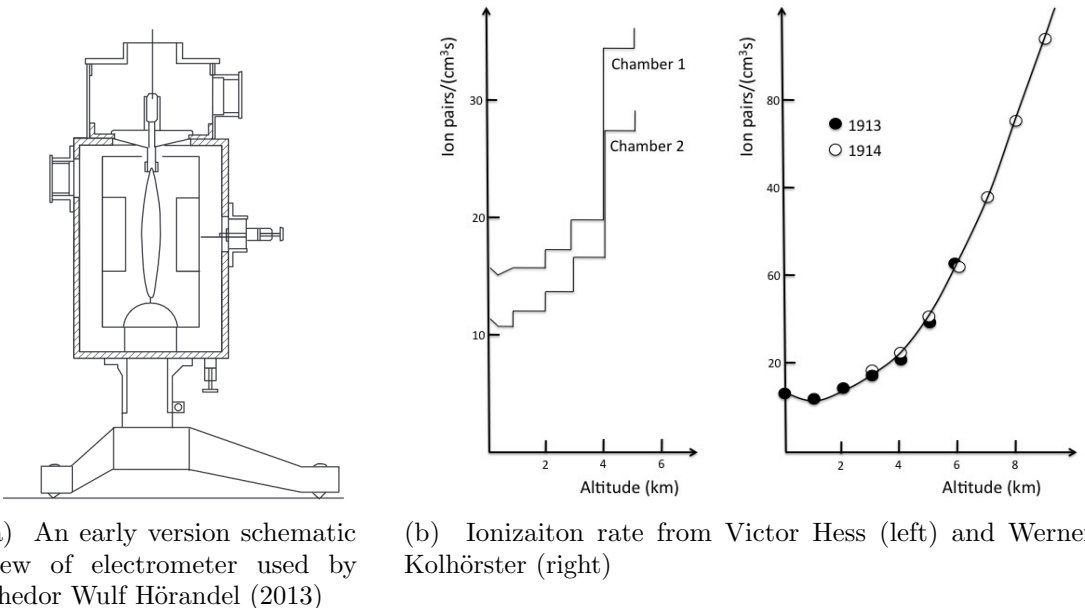


Figure 2.1: Wulf's apparatus and the balloon experimental results

However, the experiment measuring the effect of altitude variation with a tiny altitude scale compared to the Earth's atmospheric thickness may not provide enough data. They found that the ionization rate has increased by a quarter compared to that at ground level (De Angelis 2014). Three years later, a suicidal investigation was conducted by an Australian gentleman who brought a detector and himself to fly with a balloon. His name is Victor Hess, and his name went so famous because he risked his life with the experiment and his flying over 5 kilometers above the ground (Hess 1912). The result is strongly significant and impactful to the astrophysical research community. Risking life In 1914, Werner Kolhörster repeated the balloon experiment with higher altitude up to 9 kilometers from sea level and the ionization rate still increased when the balloon flew higher. These results emphasized that the source of the ionizing ray came from Earth's upper atmosphere or the outer space.

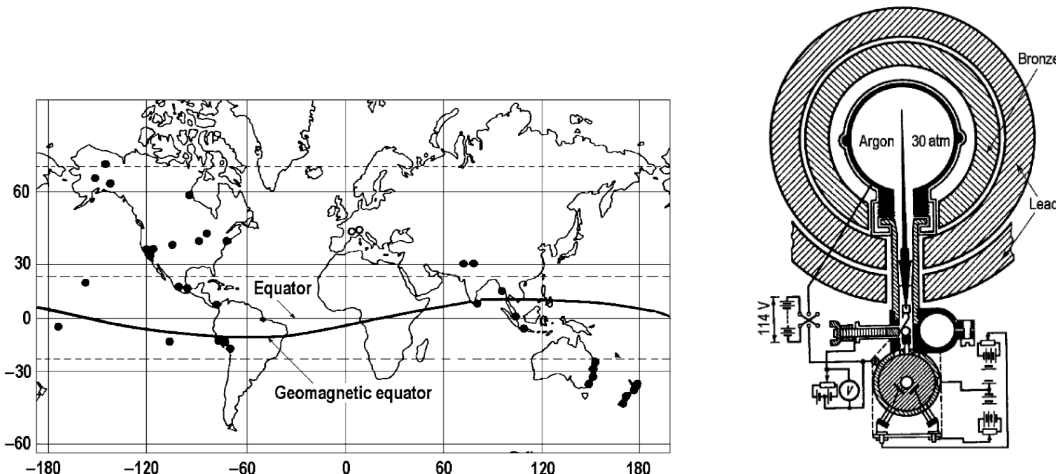


Figure 2.2: (left) Clay's experiment on the geographical variation of CR intensity. Main locations where CR intensity was measured during 8 Compton's expeditions in 1932. (right) The Pb-shielded ionization chamber, organized by Compton. Image taken from Dorman (2009)

Not only does the ionization rate varies with altitude, the measured rate also depends on the geographical locations. The first experiment was done by John Clay who sailed the ship across the ocean from Holland to Java (Clay 1927, 1928). The geographical locations where CR intensities were measured and the apparatus schematical draft are shown in Figure 2.2. The result shows that

the further from the equator, the higher CR intensity. Another exploration for the geographic variation was done by John Compton in the following five years. He sailed the ship from Sydney (southern hemisphere) to Vancouver (northern hemisphere) for various seasons during 1936 to 1937 back and forth (Compton & Turner 1937). Figure 2.3 demonstrates the latitude variation and the seasonality effects of the multiple trips from the experiment.

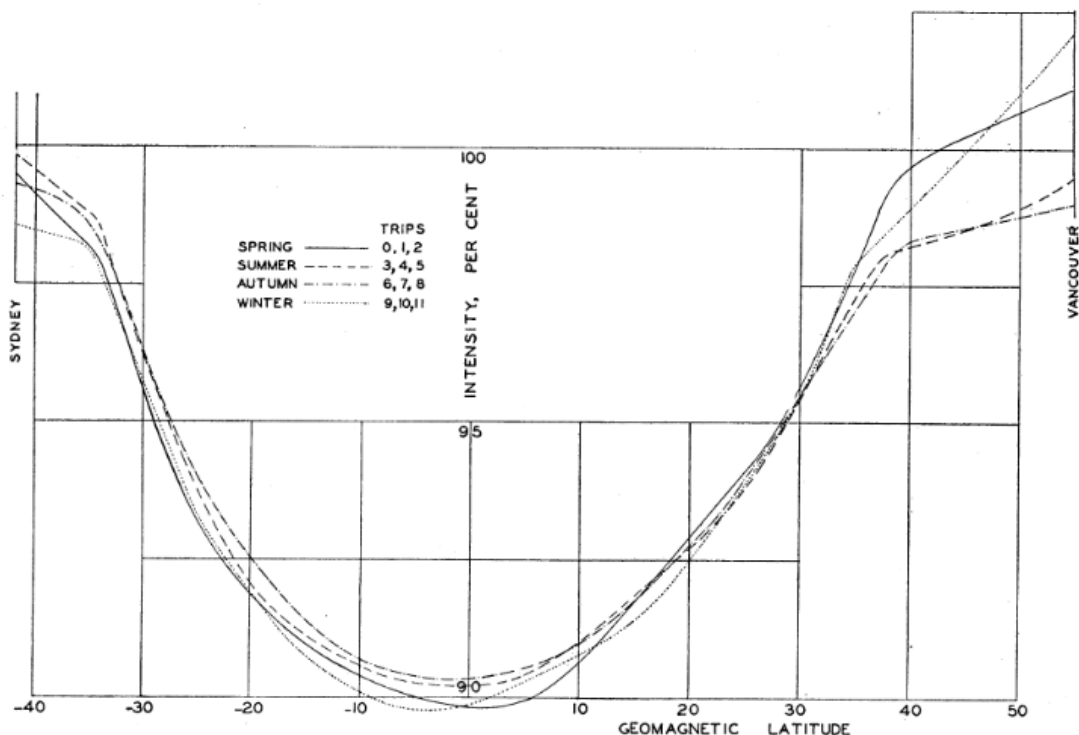


Figure 2.3: Latitude variation of CR intensity for various seasons (Compton & Turner 1937)

The first interpretation study from the discovery has been done by Störmer (1934). The explanation of the CR's altitude variation came from the trajectory of CR particles due to geomagnetic field. In that period, the topic of the geomagnetic field effects on CRs were quite famous. Another impactful study of the CR trajectories under the influence of the Earth's magnetic field was conducted by Bruno Rossi. He studied an assymetry of the East-West distribution of CR flux due to the Lorentz force effects on charged particles by the Earth's magnetic field. He found that the flux is enhanced from the West and interpreted that CRs are predominantly positively charged (Rossi & Greisen 1941).

Ground-based detectors can detect atmospheric particles from CR-air interactions. A space-based detector can also inspect the East-West asymmetry effect from a low Earth orbit. In 2008, *Fermi-LAT* was launched to observe γ rays, and also electrons, and has clearly observed the East-West effect.

2.1.2 Physical properties

CRs are high-energy particles propagating through space. CRs gain their momentum from various acceleration mechanisms CRs gain their momentum such as supernovae, created by astrophysical objects. The composition of CRs consists of approximately 90% protons, 8% alphas, and other nuclei of heavier elements (Dembinski et al. 2017). Experimentally, many observations indicate that the CR spectra for all particles and individually does follow the power law in rigidity (momentum per charge) for which the spectral index depends on the energy range. Theoretically, the observed spectrum in a broad energy range is the superposition of CRs produced by various types of sources which could exhibit different spectral indices depending on their physical properties.

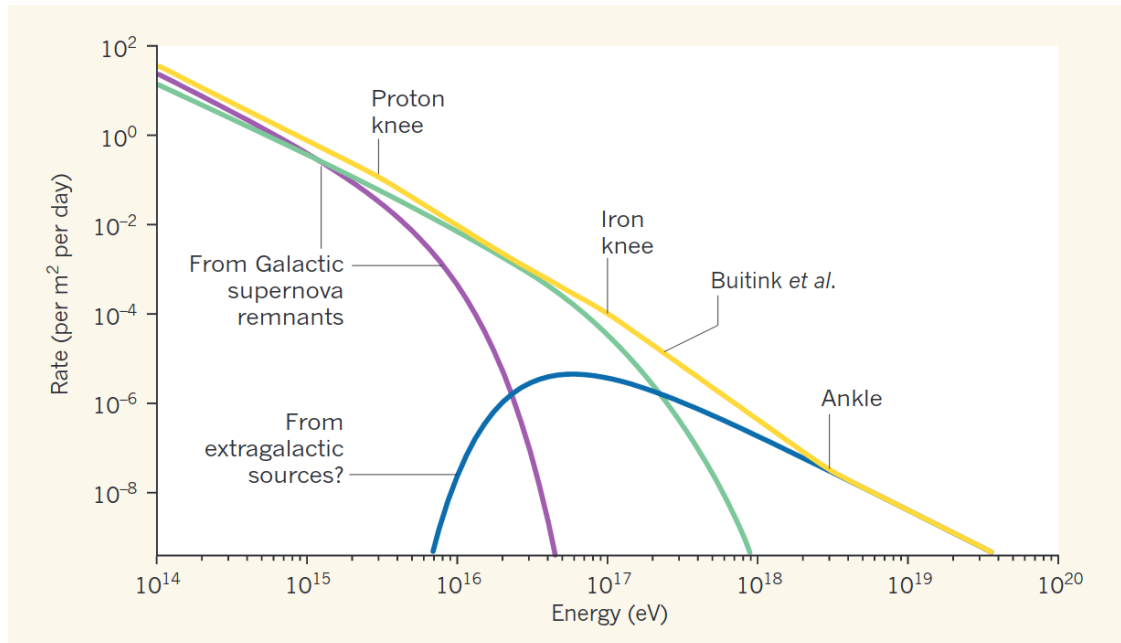


Figure 2.4: The CR spectrum showing the superposition of different populations of sources (Taylor 2016)

Figure 2.4 shows the widely accepted scenario of how each population

of CR sources dominates the value of the spectral index for different energy ranges. Three well-established spectral breaking points are the first knee at $\sim 10^{15}$ eV, the second knee at $\sim 10^{17}$ eV, and the ankle at $\sim 10^{19}$ eV. The rate to find one particle with the energy above the first knee is around one particle per square meter per year and the possibility that an apparatus could detect a particle at energy above the ankle is roughly one particle per kilometer per year.

Interestingly, the maximum energy of UHECRs ever detected never exceed ~ 2 orders of magnitude above the ankle energy. This upper energy limit of CRs is widely known as the Greisen–Zatsepin–Kuzmin (GZK limit). According to the GZK theory, UHECRs cannot have an energy above a certain limit because UHECRs are produced from distant extragalactic sources and propagate through vast space full of low-energy background photons, the cosmic microwave background. According to the GZK theory, UHECRs cannot have an energy above a certain limit because UHECRs are produced from distant extragalactic sources and propagate through vast space full of low-energy background photons, the cosmic microwave background. When the energy of the UHECRs is above a certain threshold, they would interact with the background photons and lose their energies (Greisen 1966).

CRs can be categorized into two types based on how they are produced:

1. **Primary cosmic rays:** are produced from astrophysical objects which may be within the Solar system, within the Milky Way Galaxy (Galactic CRs), or from extragalactic sources (extragalactic CRs). Some example origins of primary CRs are stellar winds, supernovae, pulsars, active galactic nuclei, and speculative sources such as dark matter decay.
2. **Secondary cosmic rays:** are produced from primary CRs interacting with the Earth's atmosphere. The interactions create showers of hadronic, leptonic, and electromagnetic particles. Researchers have developed and improved Monte Carlo simulations of the the CR air showers based on particle physics theory. These models are very useful for secondary CRs studeis.

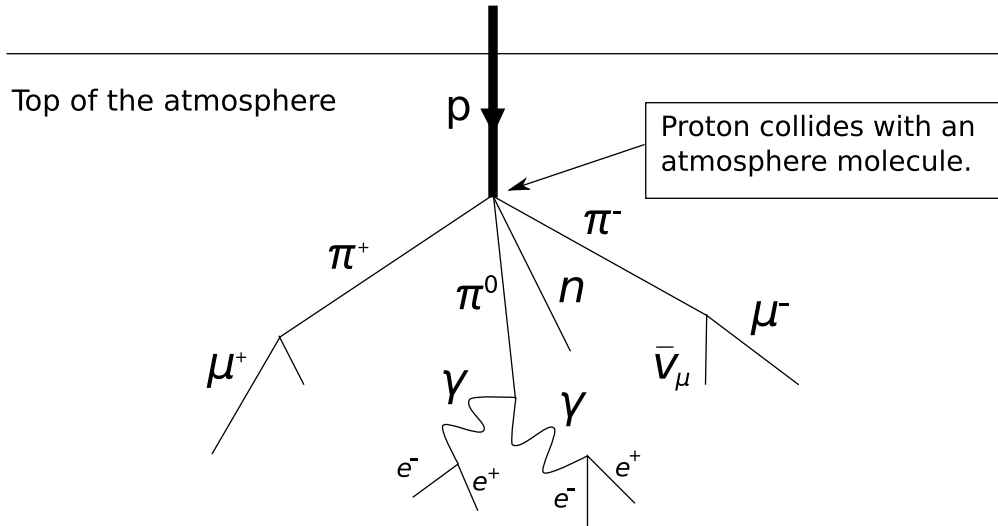
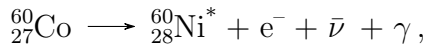


Figure 2.5: Simplified schematic of CR proton air shower (Image taken from Cosmic Rays, Wikipedia, Magnus Manske, 2011)

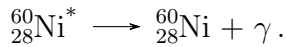
2.1.3 γ -ray production

The production mechanisms of γ rays are fundamentally different from those for charged particles which can be accelerated with the electromagnetic force. While charged particles can gain or lose energy during their propagation through space, high-energy γ -ray photons tend to only lose energy. Here we briefly discuss the production processes of γ rays.

- **Decaying of unstable matter:** Radioactive decay is one of the most well-known phenomena for the γ -decay mode. One example of heavy-ion decay is cobalt-60. It decays into an excited state of nickel as



then the excited nickel emits another γ ray to become the stable state



Some particles, such as the neutral pion (π^0), decay into γ rays. The Feynman's diagram of a π^0 decay is demonstrated in Figure 2.6. The lifetime of π^0 is short, $\sim 8.5 \times 10^{-17}$ seconds. There are some other decay channels (with $\approx 1\%$ branching ratio) which result in combinations of a photon and pairs of lightweight leptons, as long as the momentum, energy, and quantum

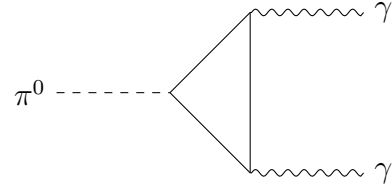


Figure 2.6: Feynman's diagram of the neutral pion (π^0) decay into two γ -rays.

numbers are conserved. Another interesting property of the $\pi^0 \rightarrow \gamma$ mode is the momentum vectors of the γ -ray pair have the same magnitude but opposite direction in the rest frame of π^0 .

- **electron–positron annihilation:** Electron (e^-) and positron (e^+) are the lightest leptons which can annihilate into 2 γ -rays. Heavier and shorter lived leptons, muon (μ) and tau (τ), can also create γ rays in a similar manner as illustrated in Figure 2.7.

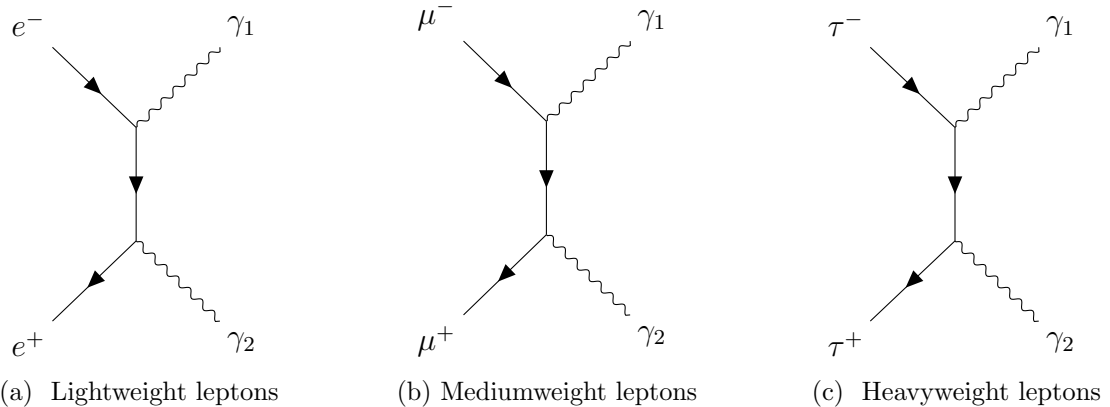


Figure 2.7: Lepton-antilepton annihilation path diagram.

- **Synchrotron & Bremsstrahlung radiation:** It is theoretically and experimentally well known that when charged particles are accelerated, they emit photons. If the acceleration is due to a magnetic field, the emission is called the synchrotron radiation. Humans have built donut-shaped apparatuses inside which charged particles are traveling in a circle guided by strong magnetic fields and produce synchrotron radiation for various applications.

Another closely related mechanism is the Bremsstrahlung process. When

charged particles, typically electrons, move close to heavier positively charged nuclei, the Coulomb force between them cause an acceleration on the electrons, resulting in Bremsstrahlung radiation.

- **Inverse Compton scattering**

scattering: A photon can electromagnetically interact with an electron (or any charged particles). The Compton scattering describes a photon losing its energy to an electron. On the opposite situation, a highly relativistic electron can interact and transfer its energy to a low-energy photon to become a γ -ray photon. This process is called the “Inverse Compton scattering” as shown in the Feynman’s diagram in Figure 2.8.



Figure 2.8: First-order Feynman’s diagrams for the Compton and Inverse Compton processes.

Astrophysical sources of γ ray

- **Supernova remnants (SNRs) and molecular clouds:** The supernova is a violent explosion of a dead star, causing material to expand in a spherical shell that sweeps the interstellar medium and decelerate over time. The shock wave from the explosion is believed to produce the shock acceleration of CRs. Three major γ -ray production processes from the SNRs involve hadronic (mostly π^0 decay) cascades, electron bremsstrahlung, and Inverse Compton scattering (Dermer & Powale 2013).
- **Diffused γ -ray emission from galactic plane:** The plane of the Milky Way galaxy has high density of gas, dust, stars, an other types of objects.

Thus, CRs can interact with such material and create diffuse emission of γ rays, which is brighter along the Galactic plane as illustrated in Figure 2.9.

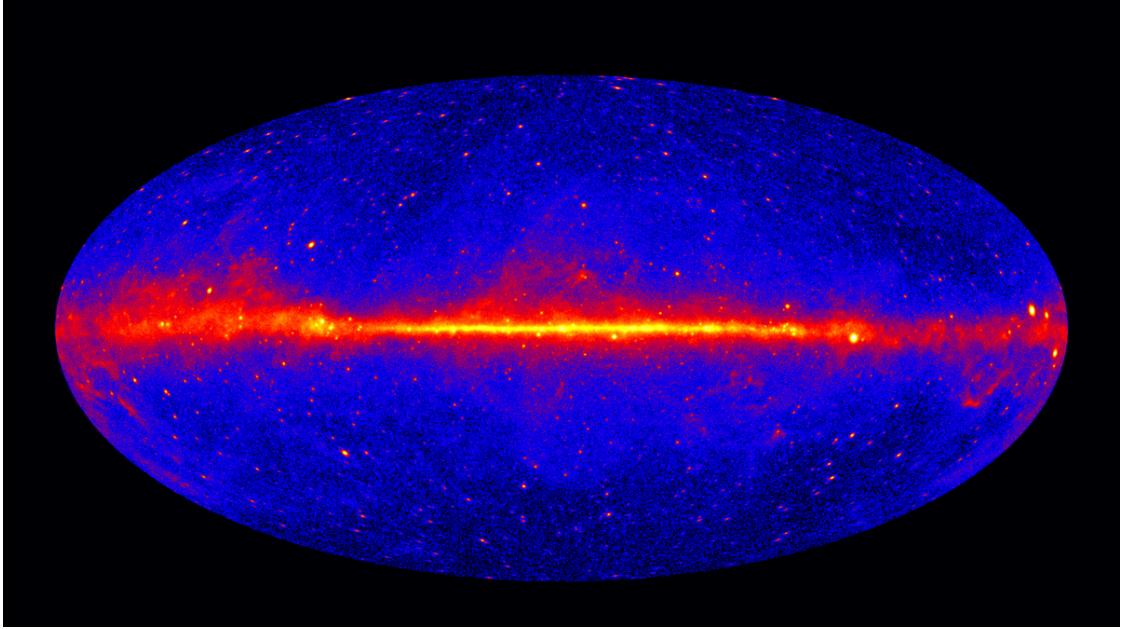


Figure 2.9: Intensity of γ -ray > 1 GeV in galactic coordinates (Image credit: NASA/DOE/*Fermi* LAT Collaboration).

- **Pulsars:** Pulsars are rapidly spinning neutron stars as a result of the supernova explosion of massive stars. They have very strong magnetic fields and can emit bright radiation in a beam from their magnetic poles. The pulsars' intensity could appear to be a periodic emission to observers on Earth due to the pulsars' rotation. They are likely the majority of point sources in the Galactic plane region detected by *Fermi* LAT.
- **Active Galactic Nuclei (AGNs):** Write this..
- **Earth's limb γ -ray production:** The closest γ -ray source to the LAT is our Earth's atmosphere. The Earth's upper atmosphere is extremely bright in γ -ray band. The Earth shines in high-energy ($\gtrsim 100$ MeV) γ ray due to the collisions of CRs with the Earth's upper atmosphere producing secondary particles which include π^0 's that quickly decay into γ rays. The Earth's γ -ray emission is the main target source for this study.

2.2 *Fermi* Large Area Telescope (LAT)

One of the famous space telescopes that observes the sky in γ -ray wavelength is the *Fermi* Large Area Telescope (LAT). Formerly, it was called Gamma-ray Large Area Space Telescope (GLAST). The LAT is designed to collect high-energy (\sim 100 MeV to above 300 GeV) photons data, but it is also able to measure electrons. The orbiting radius is around 550 kilometers from sea level. *Fermi* also carries the Gamma-ray Burst Monitor (GBM) to study γ -ray bursts for seeking exotic events. The telescope was launched on 11 June 2008 and is still currently taking data in 2021.

2.2.1 Overview

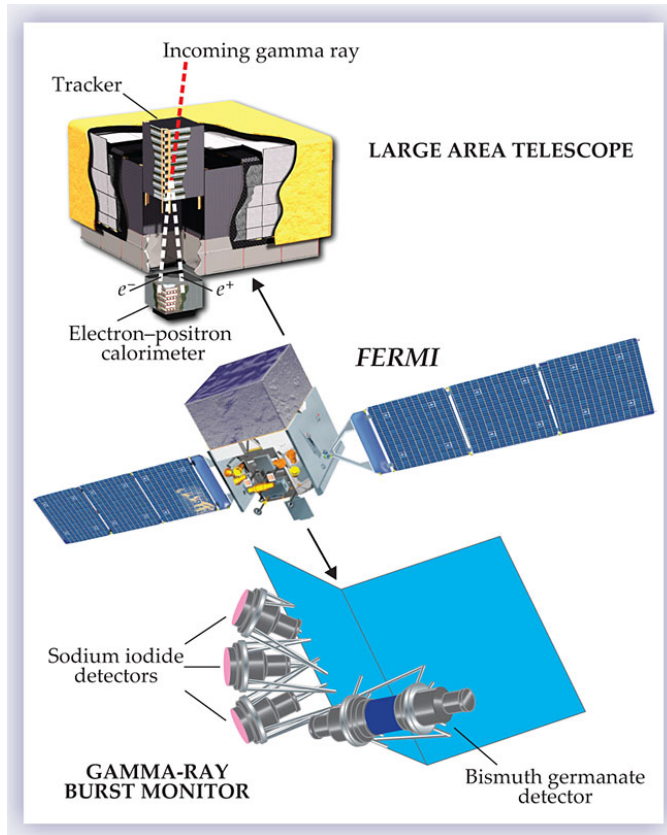


Figure 2.10: Main components of the LAT and the GBM on the *Fermi* Space Telescope (Michelson et al. 2010)

Figure 2.10 shows components of *Fermi*. There are two instruments onboard: the Large Area Telescope (LAT) and the Gamma-ray Burst Monitor

(GBM). The LAT is the primary instrument which detects γ rays between ~ 100 MeV to above 300 GeV. The GBM monitors the sky at lower energy range of ~ 8 keV to 40 MeV. The GBM consists of two sub components which are sodium iodide detector for low-energy photons (8 keV to 1 MeV) and bismuth germanate detector for high-energy photons (0.2 MeV to 40 MeV). The GBM monitors transient events and immediately triggers the LAT to point to the locations of the flares for a certain period of time before returning to the normal survey mode.

2.2.2 Large Area Telescope (LAT)

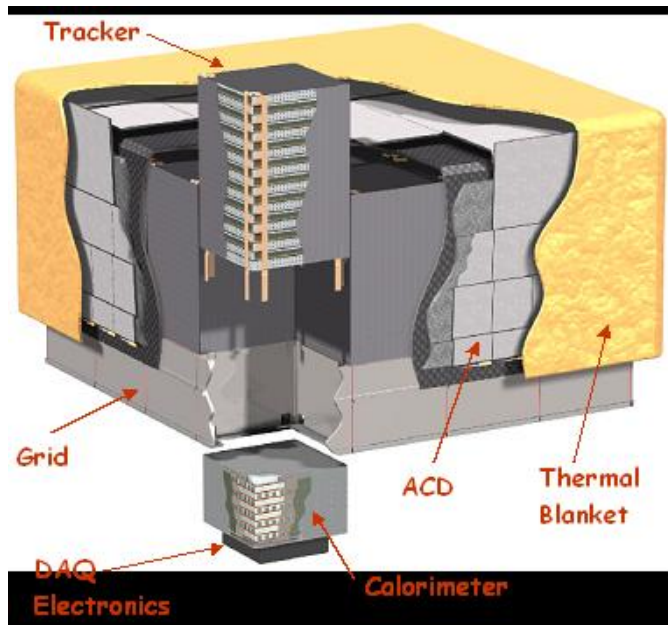


Figure 2.11: Main components of the LAT (Image taken from <https://fermi.gsfc.nasa.gov>)

Figure 2.11 illustrates main components of the LAT which are described as follows.

Anti-coincidence Detector (ACD)

The ACD consists of 89 plastic scintillator tiles covering four sides and the top of the LAT. Each tile contains two photomultipliers and wavelength shifting fibers embedded in the scintillator. The edges of neighboring tiles are overlapping to reduce the effect of the gaps. The main objective of the ACD is to reject

background charged particles which create electrical signals when passing through the scintillator tiles. The estimated efficiency for charged particle identification by the ACD is about 0.9997. **rewrite backsplash**

Tracker (TKR)

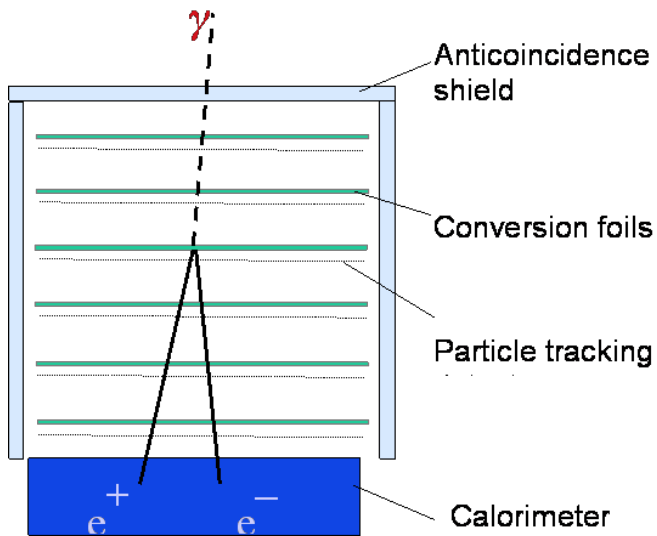


Figure 2.12: Schematic of γ -ray detection of the LAT (Image taken from <https://fermi.gsfc.nasa.gov>)

The TKR system consists of 16 planes of particle tracking detectors made from silicon strips which are interleaved with tungsten conversion foils as shown in Figure 2.12. An incident γ ray has high probability to interact with the conversion foil and is converted into an e^+e^- pair.

As the e^+e^- pair travel through the silicon strip trackers, they leave their traces on the position sensing detectors, allowing us to reconstruct the direction of the original photon. The narrow gaps between layers of silicon trackers improve the angular resolution of the LAT compared to previous instruments. In Figure 2.13, case (a) is the typical situation in which photon is pair-produced by the conversion layer and clean e^+e^- footprints are recorded. Nevertheless, there are some cases, such as (d) in which the e^+e^- paths pass through the gap between towers or (e) in which the photon is pair-converted outside of the conversion foil. Having multiple layers of trackers helps the reconstruction of these special cases.

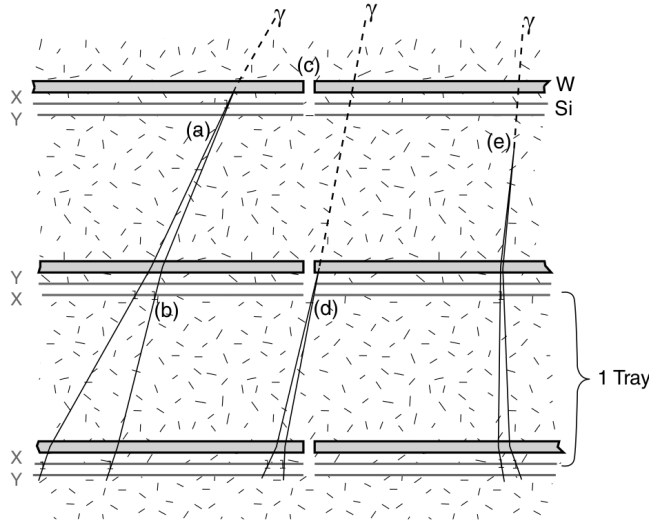


Figure 2.13: LAT's particle tracker. (a) The ideal case where the conversion happen in an early layer and leave a footprint along multiple layers (b). (c) The photon skips first layer and be converted in another layer with a missed hit in 1st and 2nd of Si trackers (d). (e) Conversion occurs in structural materials and be traced by the following Si trackers. (Atwood et al. 2009)

Calorimeter (CAL)

When the e^+e^- pair enters the CAL, they radiate their energy in the CsI crystal scintillators, producing electronic readout which is proportional to the energy loss of e^+e^- inside the CAL. According to the radiation lengths of e^+ and e^- , the CAL is optimized to contain the e^+e^- showers with energy from 0.1 to a few hundred GeV. Thus, TeV photons could have large uncertainties in their energy reconstruction by the LAT.

The overview apparatus structure is illustrated in Figure 2.14. Each calorimeter module consists of 96 CsI(Tl) scintillator crystals with the size of 2.7 cm x 2.0 cm x 32.6 cm and PIN photodiodes at both ends which connect to the readout electronic components translating the amount of light sparked in the crystal to digitized signals. Each horizontal layer is combined from 12 crystal components and stack them 8 times by rotate them 90°each for boosting the angular resolution for the sparking lights. A carbon cell was build for supporting the structure of low mass particle tracker due to the properties of high stiffness, thermal conductivity and thermal stability. An electron, position, or γ -ray will deposit the energy in

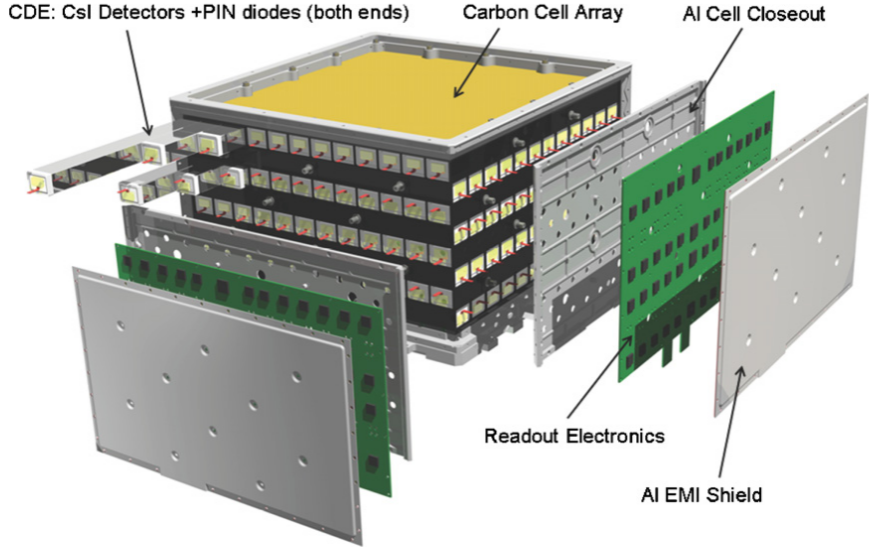


Figure 2.14: LAT's calorimeter (Atwood et al. 2009)

the calorimeter as the scintillated lights via electromagnetic interactions. The segmented crystal allow LAT to trace the showers of particles for spatial imaging.

Data Acquisition System (DAQ)

The DAQ system is designed to reduce the amount of raw data transmitted to the ground through the limited bandwidth.

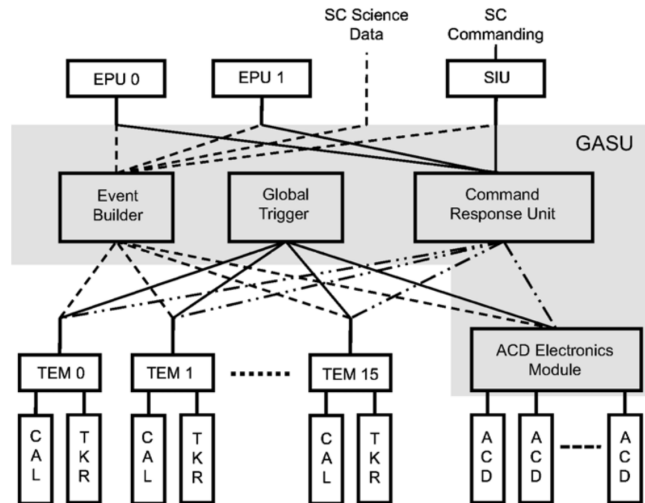


Figure 2.15: Flow chart of LAT's data acquisition system (DAQ) (Image taken from Atwood et al. (2009))

The lowest-level components are tower electronic modules (TEMs) to

serve as the interface for the the TKR and CAL. All TEMs create event buffering and communicate with the Event Builder Module (EBM) which is a component of Global-trigger/ACD-module/Signal Distribution Unit (GASU). Command Response Unit (CRU) is built to communicate the software execution in the DAQ system. Lastly, the Event Processing Unit (EPU) process a selected event from TEM and ACD Electronics Module (AEM). Filtering an event could reduce the data transmission rate from a few kHz to around 400 Hz to the ground level.

2.2.3 Event reconstruction

Before launch, the event reconstruction algorithm for photons was based entirely on the Monte Carlo (MC) simulations by modeling the photon and background signals in the ACD, TKR, and CAL systems in realistic in-orbit environment. The data processed by this pre-launch event reconstruction algorithm is called “Pass 6” version.

The raw onboard data are called “level 0”. After transmitted to the ground and processed, the data become “level 1”. After a few years after launch, the LAT collaboration have improved the event reconstruction algorithm and released the “Pass 7” version based on the actual in-flight data. The newest version and likely to be the final version is Pass 8. In each version, photons are organized into different classes (e.g., TRANSIENT, SOURCE, ULTRACLEAN, ULTRACLEANVETO) based on the level of background contamination. The TRANSIENT class has the loosest selection which allows us to obtain better statistics for the observations of faint transient sources but with a trade-off for the highest probability of background contamination. The SOURCE class is optimized for typical source analyses of the LAT, while the ULTRACLEANVETO is the cleanest class with low background contamination but also with the lowest statistics.

2.2.4 LAT performance and characteristics

Fermi LAT’s physical cross section area is $1.8 \times 1.8 \text{ m}^2$. However, its effective area for particle detection varies as a function of energy and incidence

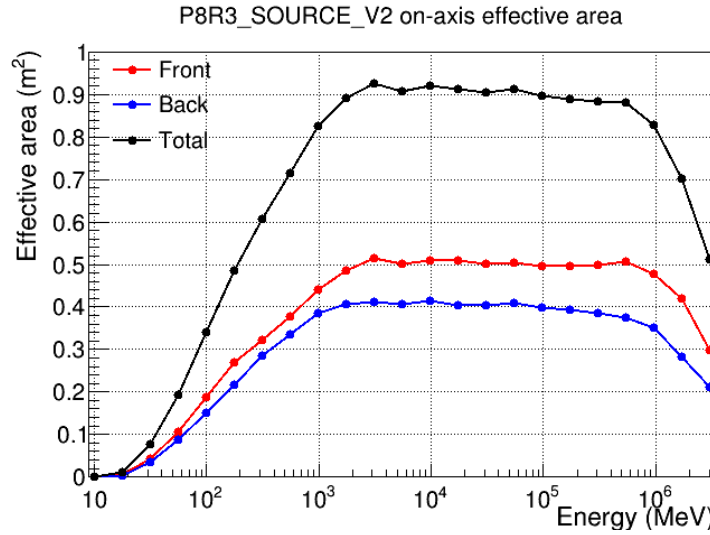


Figure 2.16: Effective area along the photon energy range from MeV to TeV (Maldera 2019)

angle. Figure 2.16 shows the LAT's Pass 8 SOURCE effective area for photons arriving perpendicular to the cross section of the LAT as a function of energy, indicating low detection efficiency below ~ 100 MeV and above ~ 1 TeV.

Another crucial variable relating to the LAT effectiveness is the incidence angle (θ_{LAT}). An event with small θ_{LAT} would pass through many tracking layers, yielding better detection efficiency. Figure 2.17 shows the relation between the effective area and θ_{LAT} .

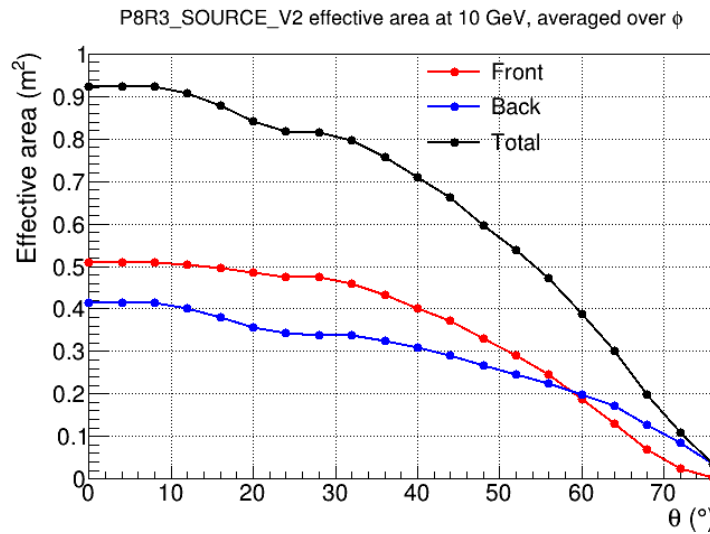


Figure 2.17: Effective area versus incidence angle (Maldera 2019)

Since the structure of the LAT is cube-like, the effective area therefore depends on the azimuthal angle (ϕ_{LAT}) of the photon. Figure 2.17 illustrates the asymmetry of the LAT's effective area as a function of ϕ_{LAT} , showing four peaks corresponding to corners of the LAT.

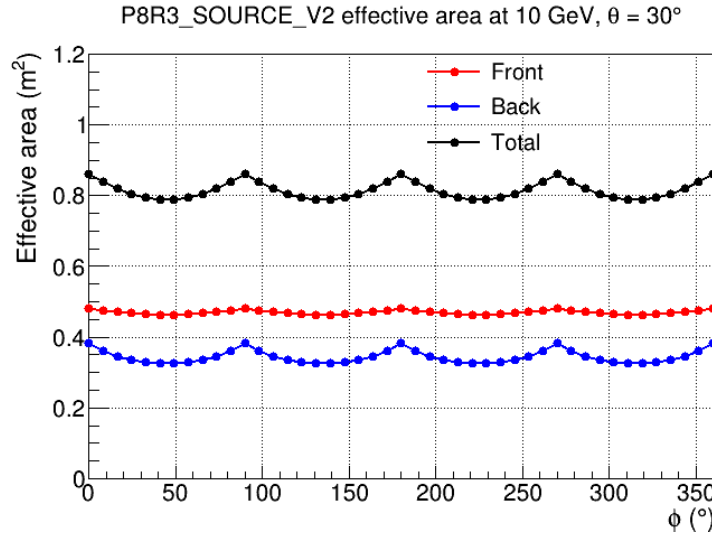


Figure 2.18: LAT's effective area versus azimuthal angle for a 10 GeV photon with the incidence angle of 30° (Maldera 2019).

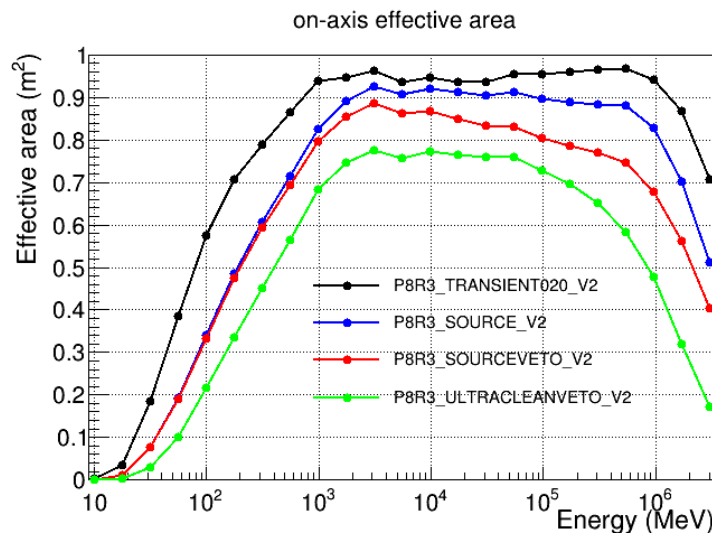


Figure 2.19: Effective area along the energy of each event class (Maldera 2019)

The event class also has a crucial role when considering the effectiveness of the reconstructed event. The cleanest class namely “ULTRACLEANVETO” would have the smallest effective area. On the other hand, the TRANSIENT class

would yield the largest effective area as illustrated in Figure 2.19.

CHAPTER III

LITERATURE REVIEW

Cosmic-ray could come from different origins from galactic sources to extra-galactic sources. The kinetic energy of cosmic rays also highly depends on where does it from. Low energy CRs usually came from the Sun called “solar energetic particle”. The production process of solar particle event mostly came from the coronal mass ejection (CME) when HZE ions were dragged by a magnetic field in the plasma. The extra-galactic CRs typically has high momentum from the extreme condition of the acceleration mechanism in pulsar, quasars and supernova remnant (SNR). The theoretical description of acceleration in SNR and solar flares is the shock wave acceleration in the following paragraph.

One of the most impactful studies of CR’s acceleration mechanism was conducted by Fermi (1949). The study describes how high energy CR particle gain such a huge momentum from the shock wave that was generated by supernovae or a great explosion from the heavy dense star. How it gains the kinetic energy could be described as a first-order shock acceleration and the overall spectrum of charged particles could be represented as the power law in Equation 3.1.

$$\frac{dN(E)}{dE} \propto E^{-\gamma} \quad (3.1)$$

where $\gamma \geq 2$ in the non-relativistic regime. However, moving magnetized plasma cloud can accelerate the charged particle in the space called “second-order Fermi acceleration”. Both regimes were computed the Lorentzian forces regardless of thermal collision in the process.

The CR protons are major components in the arrival of CR particles under multiple observations. However, α -particle is also a second important CR particle when considering a precise calculation of CR interactions. The other majority of heavy weight nuclei that could propagate through space are C, O,

Ne and so on. The differential flux in kinetic energy of multiple observations is visualized in the Figure 3.1 under the work of Beringer et al. (2012) to take various atomic numbers from various experiments.

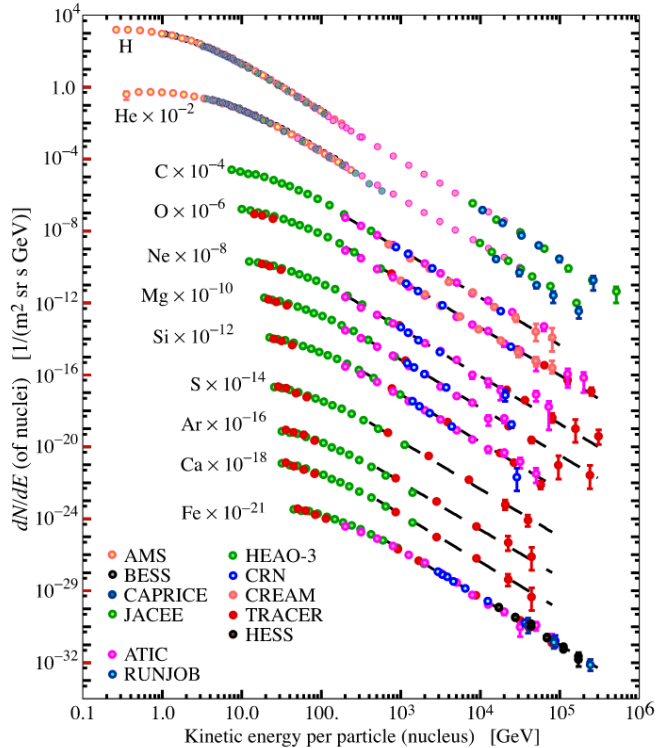


Figure 3.1: Cosmic-ray elemental spectra from various experiments (Beringer et al. 2012)

Since there is a moving plasma inside the Earth, the magnetic field has been generated from the dynamics of the moving charged ions in the plasma. The magnetic field of the Earth has a north pole at the geometric south pole of the Earth and vice versa. The Earth's magnetic field play an important role in the arrival of CR particles because the Lorentzian forces will bend the direction of a moving charged particle depends on the rigidity of the particle. This means the magnetic field line mantles the Earth with a certain direction towards the geometric north pole.

Firstly, it creates the CR cutoff rigidity on the terrestrial where each location of the Earth requires a minimum rigidity of incident charged particles as a condition for arrival. The Figure 3.2 shows a cutoff rigidity on the Earth's surface.

Secondly, incoming charged CRs with a charge has been dragged by

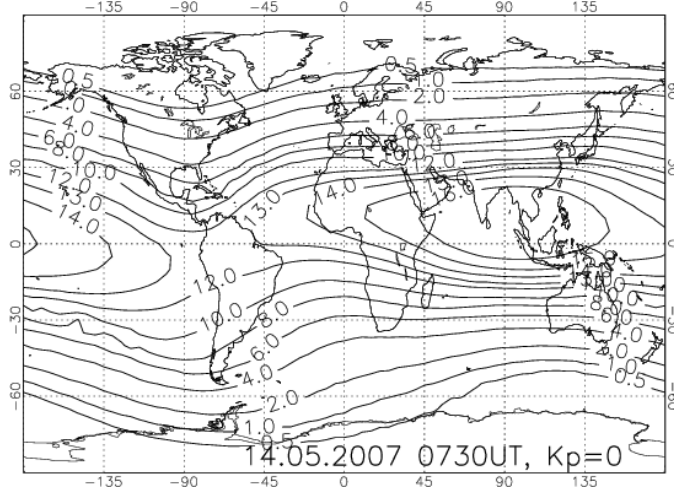


Figure 3.2: World map with computed geomagnetic vertical cutoff rigidity contour lines on a given date (B. et al. 2007)

the Earth's magnetic. Then a charged particle would move as a curve or a spiral depends on the rigidity of an incoming particle which leads to the East-West effects when an orbiting detector could find more particle on the Westside more than on the East side for a significant level of intensity. A pioneer Earth's γ -ray experiment is conducted by Kraushaar et al. (1965) where the detector was deployed on the Explorer XI satellite and orbiting in the sky.

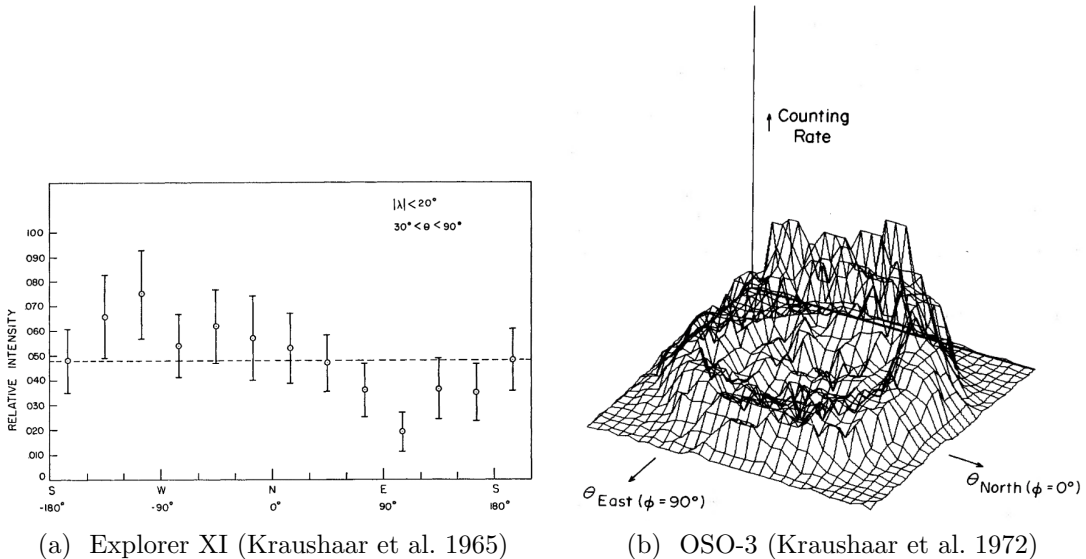


Figure 3.3: The asymmetry of γ -rays East-West intensity

The incoming photon from the East and West direction is the crucial

evidence of the bending of CRs trajectory by Earth's magnetosphere. The first analysis shows a distinguishable intensity from East to West as visualized in Figure 3.3a. The second experiment where the γ -ray detector is attached on Third Orbiting Solar Observatory (OSO-3) and collecting the γ -ray in MeV range. The 2-D plot of the intensity is shown in Figure 3.3b.

Moreover, An early analysis found that the observing γ -rays intensity along the zenith angle from different geomagnetic latitude (λ) is differentiable as shown in Figure 3.4. The reason behind this outcome came from the Earth's rigidity where the incoming particles near the equatorial have less chance to arrive than the north pole and likely to interact with the atmospheric molecules and emits the γ -rays. This is the secondary evidence of how geomagnetic fields play an important role on the trajectory of the CR particles.

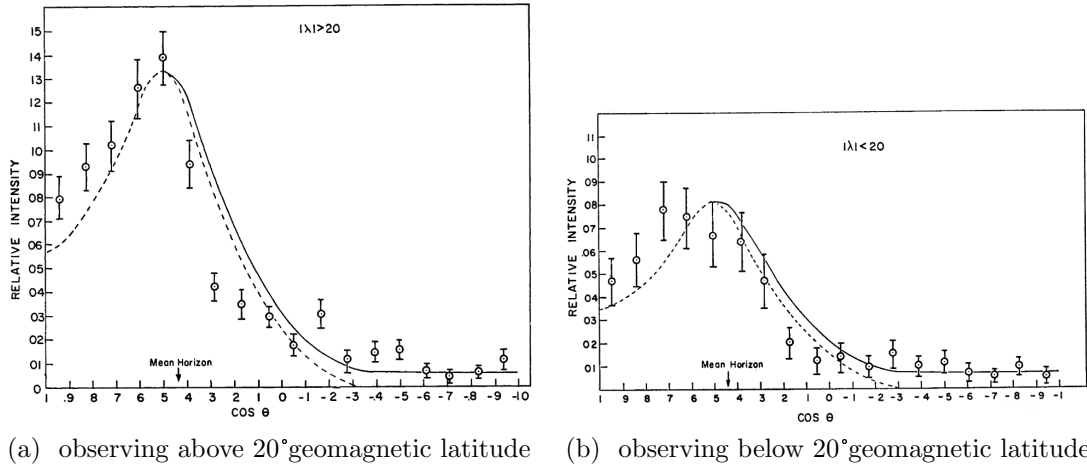


Figure 3.4: γ -ray intensity along the zenith angle (Kraushaar et al. 1965)

The following experiment of Earth's albedo observations is conducted by sending a second small astronomy satellite (SAS-2) with a higher resolution in angle and observing above 35 MeV up to GeV range (Thompson et al. 1981). The projected 3-D representation of intensity is shown in Figure 3.5a. A few decades later, another precise $\gamma - ray$ detector has been attached in the CGRO satellite (Petry 2005). An outcome from the analysis illustrated the bright region around the Earth's limb region as in Figure 3.5b.

The previous details are full of so much experimental evidence. However, Morris (1984) put the weights on the assumption of bright region as seen as albedo

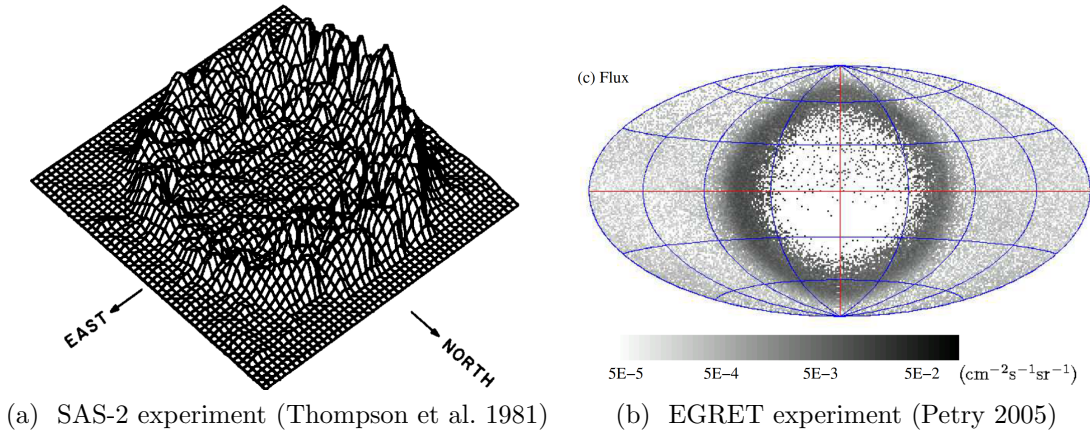


Figure 3.5: The Earth's centered intensity plot from the satellite based observations

in γ -ray came from the interaction of proton and the atmospheric nuclei. The study shows the γ -rays intensity and the variation of air depth by differing the zenith angle along limb region as plotted in Figure 3.6 and Thompson et al. (1981) data has been exploited in the analysis.

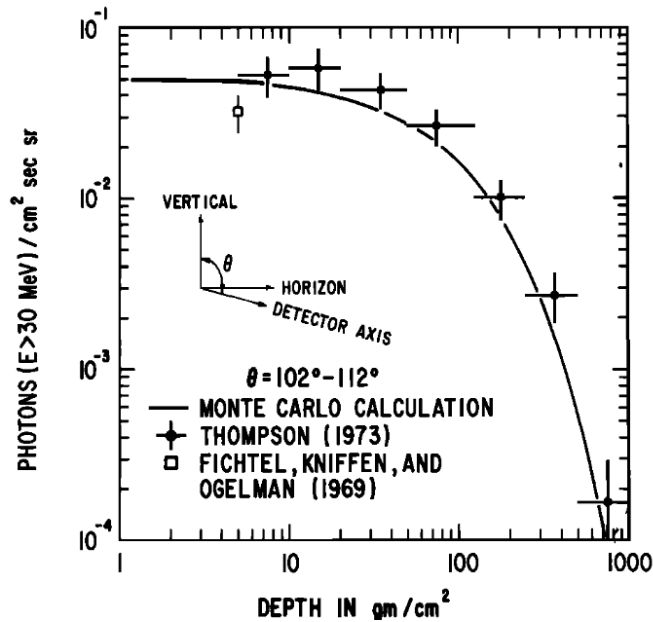


Figure 3.6: Calculated γ -ray intensity with the variation of zenithal angle (Morris 1984)

Furthermore, this study computes the γ -ray spectrum from the bright region as seen as albedo from the Earth's limb and lunar albedo. The Figure 3.7 shows the spectrum from the theoretical calculation. Figure 3.7a identify

the 2 bounds of the limb's region with an approximated air depth. Appealingly, another evidence of the solar activity could cause lower arrival CR particles since the propagating magnetic field drag a charged particle towards outer space. The distinguishable spectrum from this phenomenon is demonstrated in Figure 3.7b.

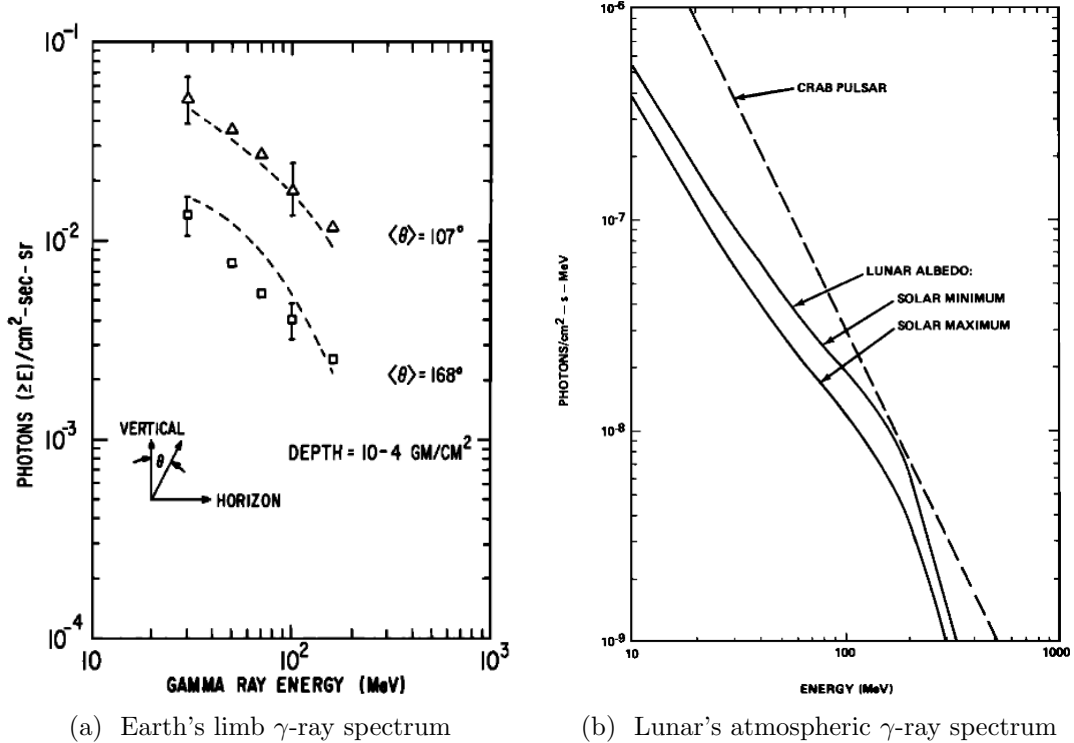


Figure 3.7: γ -ray spectrum from proton-nuclei interactions (Morris 1984)

Not so long after *Fermi*-LAT was launched in the sky. In 2009, an early examination of the induced γ -ray emission was observed by the most precise γ -ray detector Abdo et al. (2009). Since there is a huge improvement in the technological side which makes LAT capable of detecting high energy γ -ray from MeV up to TeV. Another discovery from this study was the East-West effect is highly depends on the energy where it was converted from the incident energy of CR particles. The higher energy means the higher rigidity and it would reflect how hard the magnetic field could bend the trajectory. The intensity was divided into 4 energy ranges from a few GeV to a higher GeV that could be considered as the relativistic scheme where the kinetic energy is much higher than the mass as shown in Figure 3.8.

The objective of this work is to indirectly measure the proton spectrum

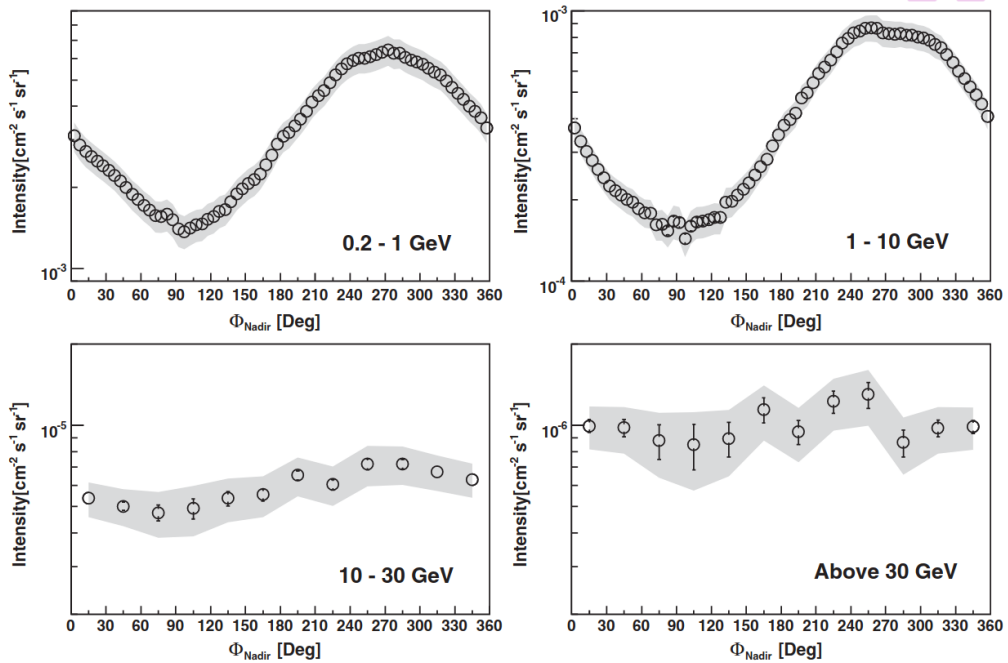


Figure 3.8: γ -rays intensity from limb emission in 4 energy ranges (Abdo et al. 2009)

in GeV range. The direct measurement in an early study of high energy CR particles such as proton and helium were observed by Haino et al. (2004). Another following experiment is Adriani et al. (2011). Both of them still lack the capability to detect such high energy on a scale of a hundred GeV. Nevertheless, there is a clue about the breaking energy in the proton spectrum with very low statistics and leaves room for further study.

Since there is just a clue from the previous direct observations. The indirect measurement of CR proton spectrum has been performed in energy between 90 GeV to 6 TeV by taking advantage of the brightness of Earth's limb from the collision of incident CR protons (Ackermann et al. 2014). The 5 years of γ -ray data have been exploited by investigating the incident proton spectrum via proton-proton collision model for finding whether CR protons have a breaking point of slope in the power law spectrum. The study found that there is a breaking spectral index in the proton spectrum above 200 GeV Nonetheles, Statistical analysis turns out that it is 1σ significant level.

Back in 2011, one of the most efficient space-based CR detectors was

launched by the carriage of Endeavor space shuttle. The detector has been attached to the international space station (ISS). The main mission of AMS-02 is to search an antimatter, dark matter from measuring CRs. It can detect antimatter such as positron and antiproton. This detector is also able to detect other heavyweight nuclei like B, CNO, Ne, etc. In 2015, a proton spectrum has been directly reported and found the breaking at 340 GV (Aguilar et al. 2015) with very high statistics. Not only the proton but the helium spectrum is also measured and reported in Aguilar et al. (2015).

According to the previous study (Ackermann et al. 2014), low statistical significant potentially came from lack of the dataset or the methodology from the consequence of indirect measurement. In this work, a similar study will be performed with a larger data size from ~ 9 years of observation. Hopefully, the study could answer the first mentioned clue and put the weights on previous work. Moreover, an improvement of the optimization process by employing the heuristic optimization as well as the high performance calculation of the exposure map for a lesser computational time in γ -ray spectrum calculation.

CHAPTER IV

METHODOLOGY

The procedure of getting data to perform an analysis from the collected data is very important. In order to get a precise Earth's limb γ -ray spectrum to trace back the incident proton spectrum, it is crucial to carefully determine the selection criteria from raw data in many angles base on the objectives. This chapter will begin by giving information on γ -ray flux extraction by providing information on data filtering and the extracting process from scratch. Secondly, the hadronic collision model that forwardly yields the γ -ray spectrum will be discussed and tracing the incident CR's proton spectrum algorithm from heuristic optimization. Lastly, the last sub-chapter contains details of statistical analysis.

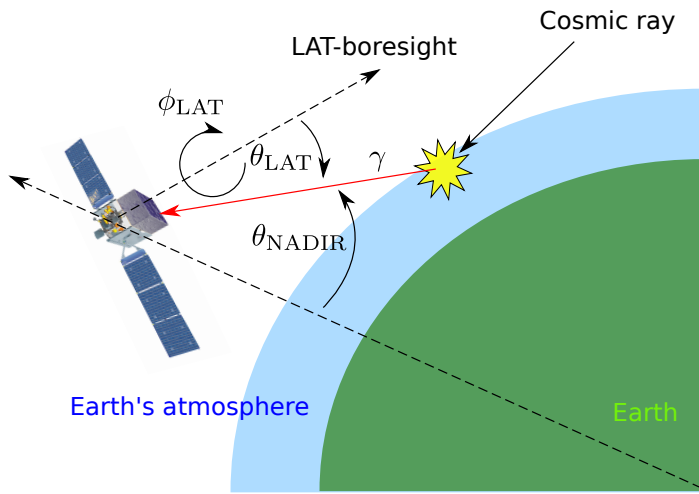


Figure 4.1: Schematics of γ -ray production

The required fundamental concept of spacecraft orientation and the observations of Earth's limb γ emission is another crucial concept. The Figure 4.1 demonstrates the important axis which is θ_{NADIR} represent the angle of how further

from Earth's center in the spacecraft point of view as well as θ_{LAT} to the angle from incident γ -ray to the detector normal in the domain between 0 to 90° and ϕ_{LAT} as the clockwise angle from 0 to 2π .

4.1 Data selection

In this work, 9 years of LAT's flight data has been used to analyze reconstructed photon and their metadata of spacecraft log recorded in a similar format periodically every half minutes. The reconstructed algorithm version is the latest version which is Pass 8 with the cleanest photon events that exist from *Fermi*-LAT data catalogs called ULTRACLEANVETO. To be more precise, the photon data is collected from publically available raw FITs file from the

Only high energy limb photon will be selected from 10 GeV up to 1 TeV. It makes the traceback analysis for gaining the information of CR proton spectrum in rigidity between 60 GV to 2 TV. The definition of γ -ray's limb region is obtained from Abdo et al. (2009) in a given nadir angle from 68.4° to 70.0° . The maximum of incident angle (θ_{LAT}) that was measured from the z-axis of the LAT's foresight is 70° .

4.2 Flux extraction

There are multiple steps from trivial to the complex calculation to obtain the differential flux. The definition when saying flux is a differential flux that is calculated one chunk of energy range at a time as Equation 4.1.

$$\text{Flux} \equiv \frac{dN_\gamma}{dE} = \frac{\int_{\text{Limb region}} (\text{Count map}/\text{Exposure map})}{\Delta\Omega\Delta E}. \quad (4.1)$$

Since the CR spectrum follows a power law as the exponential form $dN/dR \propto R^\gamma$ as mentioned in the background section. Then the log-log relation of the flux versus rigidity would behave like a trivial linear trend in the plot. Not only the rigidity but in the high energy CR like 10 GeV also makes the energy of the particle almost

the same as the rigidity does. Consequently, the γ -ray spectrum is equally divided in the energy space in the log scale for 50 bins.

To get the spectrum, it is obvious to construct the histogram with 50 bins in a given energy scale as explained in the previous paragraph. The flux of each bin could be computed separately by initializing the empty count map and the exposure map where it represents the exposure time and the effectiveness of the spacecraft when looking at each angle in the sky. Let regards the following example for a deeper understanding. The ideal scenario is when incident γ -ray walk pass through the LAT in a normal line of the detector. The performance would be the highest it could do. On the other hand, if the incident γ -ray arrives with high tile angle from the LAT's plane (High θ_{LAT}). An angle resolution is selected to be 2° in ϕ_{NADIR} and 0.1° in θ_{NADIR} . The reason behind these number is simply from the toy experiment of plotting the result in the 2D histogram and it is selected to be the one as the bin value is not too noisy. In another word, it should not be too small so that the result is not too noisy and it is should not so big due to the limb region could not be seen clearly which leads to the matched photon mixed up with the Earth's γ -rays and collecting too many primaries CR photon.

Basically, the procedure is summarized in these following steps.

1. Make 2D histograms with 25 bins per decade of energy
2. Select photon data and fill in the 2D histograms
3. Calculate exposure maps which include the effective area and livetime of the LAT as it observed the Earth
4. Compute the flux by applying Equation 4.1 in for bin
5. Taking consider background subtraction from a average uniform background photon distribution by treating bin by bin

4.2.1 Exposure map gathering

In fact, step 3 is the most complicated stage in this work. Practically, *Fermi*-LAT was designed for observing the space which makes the spacecraft

logging in equatorial coordinates, not for the Earth's polar coordinates. The LAT position is recorded in equatorial coordinates as well as the LAT's boresight of the detector plane to log their orientation during the orbit. At the end of the day, the coordinates transformation would be performed from multiple frame of reference to LAT boresight for acquiring the exposure of LAT's FoV and reference the effectiveness from LAT's boresight angle dependency. The following content is the full detail of how things going on under the hood.

Coordinate Transformations

Firstly, the spacecraft orbit is recorded in the equatorial coordinate which in a spherical point of view. Defining the cartesian coordinate that share the origin between the celestial point of view and the spacecraft by letting one axis point to the spacecraft could assist the calculation more conveniently as the Figure 4.2. Please note that the x-axis in the equatorial coordinate is called "Equinox".

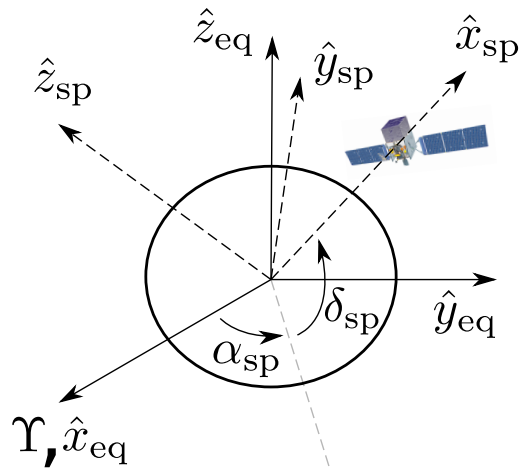


Figure 4.2: Coordinate transform between celestial and spacecraft

However, mapping into the cartesian coordinate by adopting a unit vector in 3 dimensions has been written as Equation 4.2 and the symbolic transformation is represented in Equation 4.3.

$$\begin{aligned}\hat{x}_{\text{sp}} &= \cos \delta_{\text{sp}} \cos \alpha_{\text{sp}} \hat{x}_{\text{eq}} + \cos \delta_{\text{sp}} \sin \alpha_{\text{sp}} \hat{y}_{\text{eq}} + \sin \delta_{\text{sp}} \hat{z}_{\text{eq}} \\ \hat{z}_{\text{sp}} &= -\sin \delta_{\text{sp}} \cos \alpha_{\text{sp}} \hat{x}_{\text{eq}} + \sin \delta_{\text{sp}} \sin \alpha_{\text{sp}} \hat{y}_{\text{eq}} + \cos \delta_{\text{sp}} \hat{z}_{\text{eq}} \\ \hat{y}_{\text{sp}} &= \hat{z}_{\text{sp}} \times \hat{x}_{\text{sp}}\end{aligned}\quad (4.2)$$

$$\hat{r}_{\text{sp}} \equiv T_{\text{eq} \rightarrow \text{sp}}(\delta_{\text{sp}}, \alpha_{\text{sp}}) \hat{r}_{\text{eq}} \quad (4.3)$$

The transformation matrix $T_{\text{eq} \rightarrow \text{sp}}$ has been implemented as a matrix in practical analysis due to the convenience for calculation and the compaction in the programming point of view.

Secondly, LAT's boresight coordinates are also referenced in equatorial coordinates. Figure 4.3 demonstrates the relation between an incident plane of the detector on equatorial coordinate and the nadir angle regarding the exposure from LAT to Earth.

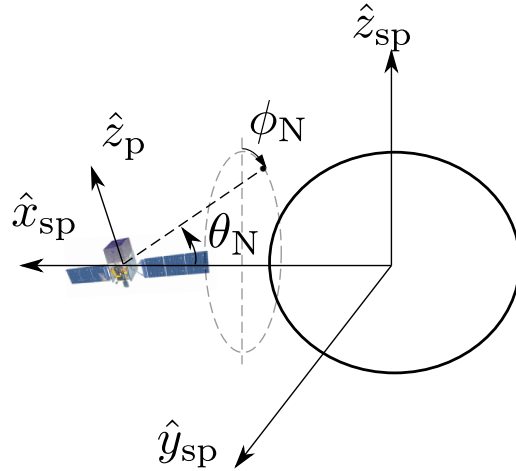


Figure 4.3: Coordinate transform between spacecraft and nadir angle

Unquestionably, it has to be converted into a cartesian point of view to do a mathematical operation for simplicity. A full representation of the coordinates could be written as Equation 4.4 and the compact form is in the Equation 4.5.

$$\begin{aligned}\hat{x}_p &= \cos \delta_p^x \cos \alpha_p^x \hat{x}_{eq} + \cos \delta_p^x \sin \alpha_p^x \hat{y}_{eq} + \sin \delta_{sp}^x \hat{z}_{eq} \\ \hat{z}_p &= \cos \delta_p^z \cos \alpha_p^z \hat{x}_{eq} + \cos \delta_p^z \sin \alpha_p^z \hat{y}_{eq} + \sin \delta_{sp}^z \hat{z}_{eq} \\ \hat{y}_p &= \hat{z}_p \times \hat{x}_p\end{aligned}\quad (4.4)$$

$$\hat{r}_p \equiv T_{eq \rightarrow p}(\delta_p^x, \alpha_p^x, \delta_p^z, \alpha_p^z) \hat{r}_{eq} \quad (4.5)$$

Similarly, $T_{eq \rightarrow p}$ is also considered as a transformation matrix in the computation for monotizing the source code as well as keeping consistency in the logic.

Again, all those representations just for mapping the LAT's boresight coordinate to link with the nadir coordinate to accumulate the exposure from the spacecraft's FoV. The spacecraft coordinate can be written as a dependency of Earth's polar coordinate as Equation 4.6 in the cartesian system.

$$\hat{r}_{sp}^o(\theta_N, \phi_N) \equiv -\cos \theta_N \hat{x}_{sp} + \sin \theta_N \cos \phi_N \hat{z}_{sp} + \sin \theta_N \sin \phi_N \hat{y}_{sp} \quad (4.6)$$

By the end of the day, extracting the relations to simplify the LAT's boresight coordinate could be contained by one inversion of transformation matrix from equatorial to spacecraft and transform it to plane of the detector as written in the compact form in the Equation 4.7.

$$\hat{r}_p^o(\theta_N, \phi_N) = T_{eq \rightarrow p}(\delta_p^x, \alpha_p^x, \delta_p^z, \alpha_p^z) [T_{eq \rightarrow sp}(\delta_{sp}, \alpha_{sp})]^{-1} \hat{r}_{sp}^o(\theta_N, \phi_N) \quad (4.7)$$

Geometrically, an angular coordinate of the LAT plane could be obtained from a normalized component of the cartesian unit vector as in Figure 4.4. The exposure accumulation has been calculated in every single grid from the previous relation.

Parallel Computations

From the previous section, it is obvious that the complexity of the code becoming large due to the transformation operation. For example, a plain matrix

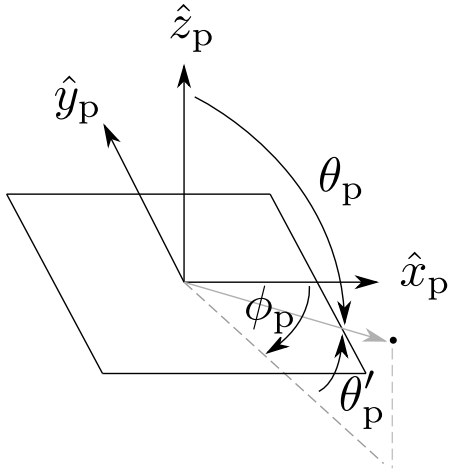


Figure 4.4: Detector’s boresight in cartesian and polar coordinate

inversion cost $\mathcal{O}(n^3)$ where n is 3 because it is a 3 by 3 matrix in this case. Not only the inversion, but the matrix multiplication also cost the same amount of complexity which causes a long run in the execution time because the original program has been designed in sequential execution.

Nevertheless, the spacecraft log file namely “FT2” has been recorded row by row which equivalently to a CSV format as a plain table with the specific columns. Since the objectives are to determine the exposure map by counting the exposure time as well as the effectiveness of the spacecraft from each angle for a given small range of energy which means that the energy could be approximate as one energy for getting the effective area in each angle of the LAT during calculation. Moreover, the exposure could be calculated parallelly for each step or in each row of the FT2 due to the property of the exposure map. Consequently, splitting the exposure map and calculate parallelly is possible to get rid of the performance issue.

The code is implemented in Message Passing Interface (MPI). The framework provides a simple protocol without knowing any type of protocol or zero required network knowledge. It assists the user to freely control multiple processes with full control of each process. According to Flynn’s taxonomy of computation, this work exploits the Multiple Instruction Multiple Data (MIMD) architecture to utilizing the resources in a distributed systems.

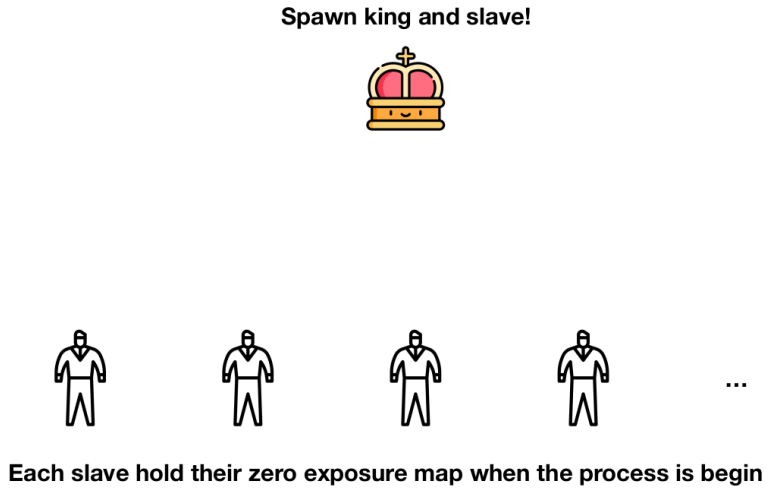


Figure 4.5: Spawning the king and slave processes

To begin with, the calculation, initializing the exposure map with a separate workers and send multiple rows to the workers in the same amount is trivial and waste a lot of resources since there will be a fast worker who do a calculation fast and the slow worker due to the cluster is composed of non-monolithic nodes with different performances. The trivial calculation will lock the resource in the cluster and blocks the other researcher who wants to run because of the resource allocation issue. To maximize the usage of the CPU-based cluster computing, there is a mechanism called the “Master-Slave technique”. The algorithm has been designed for utilizing the resource by spawning a king as the process manager and multiple slaves to be a process worker. The starting process could be demonstrated in Figure 4.5.

After that, the FT2 rows will be sent to slaves sequentially until all workers hold a small chunk of data and do their jobs. In practice, there is metadata attach to the message. One of the options is the status tag. The status tag sends to the worker to declare the state of the process whether it is in the calculation or the finishing. Figure 4.7 illustrates the non-sequential sending of the workload. The idea is simply sending a small task to an available worker and skip a busy worker without disturbing them. This mechanism allows the execution to utilize the resource in the cluster without wasting in the free worker.

By the end of the day, if the task is completely sent. The master process

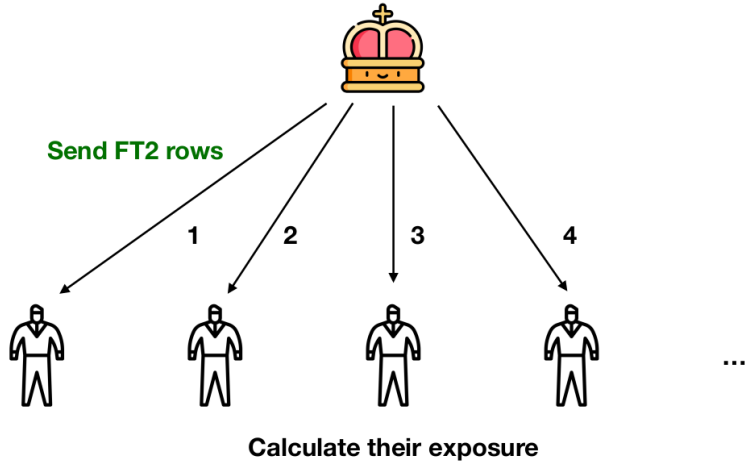


Figure 4.6: Master process send a small task to workers

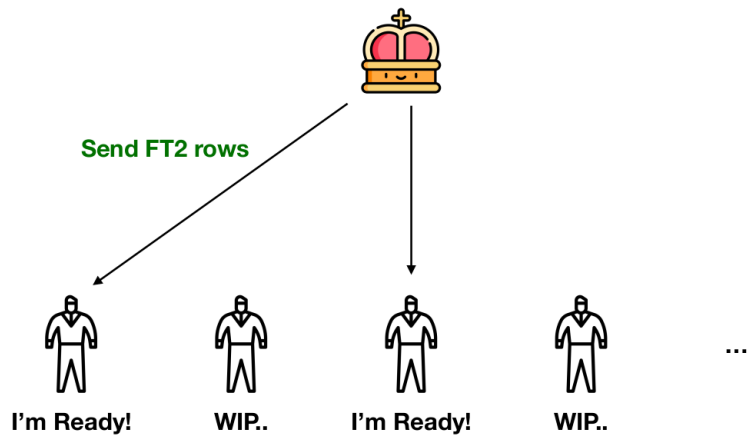


Figure 4.7: Asynchronous sending to an available worker

will send the status tag as done to be an announcement of the finishing period. Then the exposure map of each worker will be gathered in the master process for superposition and dump it to unify an exposure map. In addition, the calculation in an early period of testing is reported in Appendix A.

4.3 Hadronic Collision Model

The proton spectrum power law in rigidity is described in Equation 4.8 as a single power law (SPL) where the γ represents the spectral index of the

model. In fact, the spectrum has been observed as the differential flux in energy. Converting process between the rigidity spectrum and the energy spectrum is derived in Appendix B to obtain a precise calculation.

Single power law (SPL)

$$\frac{dN}{dR} = R_0 R^{-\gamma} \quad (4.8)$$

The most crucial part of this work is to determine if there is any breaking in the spectral indices in the power law. To represent a single breaking energy, the broken power law (BPL) could be modeled the spectrum in rigidity as Equation 4.9.

Broken power law (BPL)

$$\frac{dN}{dR} = \begin{cases} R_0 R^{-\gamma_1} & : E < E_{\text{Break}} \\ R_0 [R(E_{\text{Break}})]^{\gamma_2 - \gamma_1} R^{-\gamma_2} & : E \geq E_{\text{Break}} \end{cases} \quad (4.9)$$

The scattering process of the hadronic collision from proton hitting the atmospheric molecules. The collision from incoming proton kinetic energy above 10 GeV could be modeled by proton-proton collision with an approximation that depends on the majority of the air components. Model for the collision of proton-proton which yields γ -ray as a secondary product as a distribution in the spectrum has been derived in Equation 4.10 from Kachelrieß & Ostapchenko (2012) work.

$$\frac{dN_\gamma}{dE_\gamma} \propto \int_{E_\gamma}^{E_{\max}} dE' \frac{dN_p}{dE'} \frac{d\sigma^{pp \rightarrow \gamma}(E', E_\gamma)}{dE_\gamma} \quad (4.10)$$

Where $d\sigma^{pp \rightarrow \gamma}(E', E_\gamma)/dE_\gamma$ contains a scattering amplitude of a given kinetic energy proton and the spectrum of the γ -ray. Atmospheric components mostly consists of nitrogen as the majority and the oxygen (Wallace & Hobbs 2006). The cross-section from proton-proton collision and proton-nitrogen collision is roughly approximate as the multiplicative relation since there is plateau curve in the energy range in this analysis. The relation of the proton-proton scattering amplitude and the proton-nitrogen is obtained from Atwater & Freier (1986a) where it highly depends on the atomic numbers of the air molecules.

However, the second highest fraction of the arrival CR particles on Earth is an alpha (α) particle. The helium nuclei can interact with the nitrogen and produce high energy γ -rays depends on how much kinetic energy α -particles is holding. Another estimation has been exploited by applying $\sigma_{\alpha N}/\sigma_{pN}$ to be a constant around 1.6 at the energy range in GeV from the same relationship of the proton-air collision model. Hence, derived equation of the scattering process from incoming proton and α -particle with air molecules to produce γ -ray spectrum could be shown as Equation 4.11

$$\frac{dN_\gamma}{dE_\gamma}(E_\gamma) \propto \sum_{E'_i} \left[\frac{E'_i}{E_\gamma} \Delta(\ln E'_i) \right] \left[f_{pp} \frac{dN_p}{dE'_i} \left\{ 1 + \frac{\sigma_{HeN}}{\sigma pN} \left(\frac{dN_p}{dR} \right)^{-1} \frac{dN_{He}}{dR} \frac{dR_{He}}{dR_p} \right\} \right], \quad (4.11)$$

The CR helium spectrum would not be measured in this work since there will be multiple parameters that leads to an overwhelming local optimum. The spectrum of α -particles is directly measured by Aguilar et al. (2015) and fix the distribution as one function rather modeled spectrum of CR proton spectrum. The full detail of the equation derivation will be demonstrated in D.

4.4 Optimization

Determining the best-fit spectral model requires an objectives function to represent how well the model match with an observed data. A proper methodology for fitting or optimization in another word is also a crucial part since it is likely that the local optimum exists in the parameters space. A poor optimization could lead the best-fit stuck in a local minimum and yield a poor result. For better escaping local optima, heuristic optimization is employed for finding the best-fit of the model in parameter space.

Poisson likelihood function

An objective function is defined as Poisson likelihood function in the Equation 4.12. The reason behind the selection of the Poisson function came from

the observed model and measurement is considered as a number of photons in each bin of the histogram. Converting the model spectrum to be a count histogram is simply multiplied by the integral of the exposure map in the limb region.

$$\mathcal{L} = \prod_{i=1}^N P_{\text{pois}}(n_{i,\text{model}}, n_{i,\text{measurement}}) \quad (4.12)$$

Since the spectrum order is in different order of magnitude, then a proper way to define an objective function is to redefine a likelihood as a log-likelihood function for numerically convenient like Eq 4.13.

$$Sum = \sum_{i=1}^N -\log P_{\text{pois}}(n_{i,\text{model}}, n_{i,\text{measurement}}) \quad (4.13)$$

To sum up, a given proton spectrum yield a distribution of γ -ray spectrum to be converted into a count histogram and comparing with the real measurement. Not only for numerical convenient but the negative sign also makes an algorithm to minimize the system rather than maximize a likelihood.

Particle Swarm Optimization (PSO)

In the early phase of the optimization, a plain gradient descent optimization has been used for model fitting. The result turns out that with different initial parameters, the different best-fit model has changed which implies the local minimum in the problem. Even there is no method to guarantee the global minimum but the heuristic optimization could be a better option for handling this type of problem. One kind of most widely used algorithm is particle swarm optimization (PSO) and it is invented by Kennedy & Eberhart (1995).

In order to get a best fit spectral indices, employing the Particle Swarm Optimization (PSO) by randomly initiate many particles in a given range of the parameter space and find the local and global best fit in each step of the iteration. Then rest of them would slowly move toward to the local and global position in parameter space with a proper weight. The iteration process will stop when the standard deviation of the objective function from every particle less than a decimal. The explicit formula for every iteration k , particle i move with velocity v_k^i is

$$v_{k+1}^i = \omega v_k^i + c^b r_k^b [b_k^i - x_k^i] + c^B r_k^B [B_k^i - x_k^i], \quad (4.14)$$

and updating the particle i with

$$x_{k+1}^i = x_k^i + v_{k+1}^i. \quad (4.15)$$

where

- x_k^i represent variable that particle i hold
- b and B are best local and global parameter sets along the optimization process
- Set $\omega = 0.2$, $c^b = 0.2$ and $c^B = 0.3$

4.5 Statistical significance

Certainly, larger model parameters or complexity would yield a better performance except it is overfitting the problem. The critical issue is to answer how much significance the alternative model could outperform the trivial model. As the language of statistics would consider as two hypotheses. One for null and one for alternative approach.

For this case, BPL has 2 more degrees of freedom (DOF) than SPL. Unquestionably, if there is a good optimization procedure, the objectives function would say BPL is better SPL. As mentioned from the previous paragraph, the significance level has to be taken into account to put the weight on the study. Theoretically, regarding the model likelihood with a given set of parameters could be determined in the general case as Wilk's theorem define the relation in Equation 4.16.

$$\mathcal{L} \equiv \prod_{\alpha=1}^n f(x_\alpha, \theta_1, \theta_2, \dots, \theta_h) \quad (4.16)$$

where

- x_α is represent a variant from model and data

- θ_i is a degree of freedom (DOF)

The practical usage to compare the null hypothesis and the alternative hypothesis as similar to one-tail hypothesis testing with a given dependency in more DOF has been adopted by Huelsenbeck & Crandall (1997). This method called “Likelihood ratio test (LRT)”. The compact formula is shown in Equation 4.17.

$$\text{LRT} = -2 \ln \left(\frac{\mathcal{L}_{\text{null}}}{\mathcal{L}_{\text{alternative}}} \right) \quad (4.17)$$

CHAPTER V

RESULTS AND DISCUSSION

The content of this chapter would be reported as the analysis procedure from step one to the end. The first part is the data correction process, count maps from the raw count as well as exposure map from the parallel computation, the spectrum and inversion model fitting by heuristic optimization.

5.1 Limb's angle correction

Theoretically, the peak profile of the θ_{NADIR} would be the same. From the observations, the nadir angle change through time evolving since the spacecraft altitude is gradually getting lower in each year which will affect the LAT point of view when it sees the Earth.

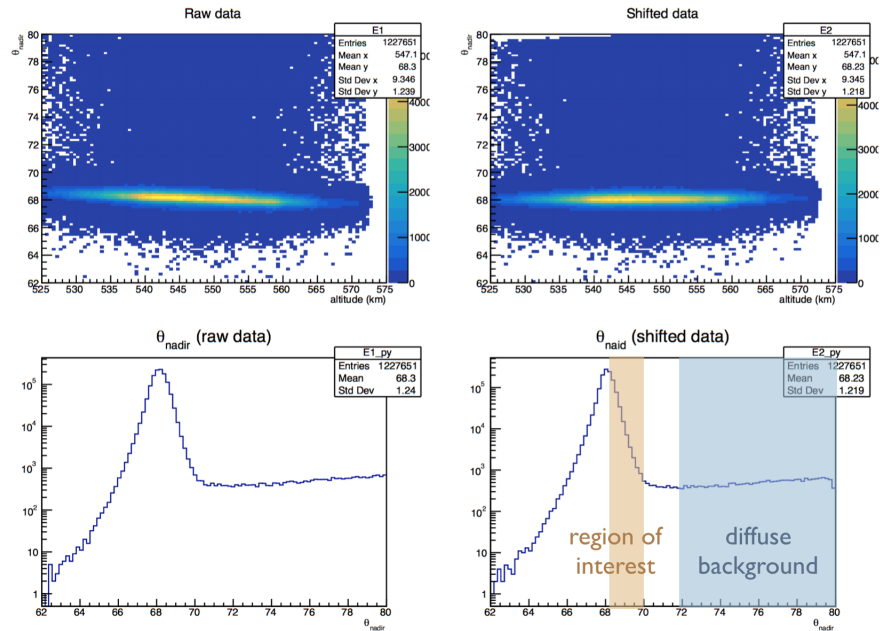


Figure 5.1: Distribution of nadir angle before and after altitude correction

The top-left of Figure 5.1 demonstrates how much spacecraft orbiting

altitude correlate to the θ_{NADIR} by a 2D heatmap plot of photon intensity. The bottom-left histogram came from the projection of the previous raw count 2-D histogram which has a peak around 68° . Both bottom and top right histograms was constructed from exactly the same logic but there is one different variable. The shifted nadir angle has been calculated to reduce the effect from the spacecraft and the region of interest has been highlighted as orange for calculating as the limb spectrum and the blue zone is a diffusive background to be used in the background subtraction.

The brightness of Earth's limb is much brighter than the diffusive background on the map. The region of interest and the background intensity has a huge difference in approximately an order or magnitude.

5.2 γ -ray spectrum measurement

According to the definition from Equation 4.1, the first step is the construction of the count map of the Earth's centered coordinates. Regardless of the photon energy, a week of the accumulated photon has been plotted in the Figure 5.2 to visualize the raw count of the sample data on the count map.

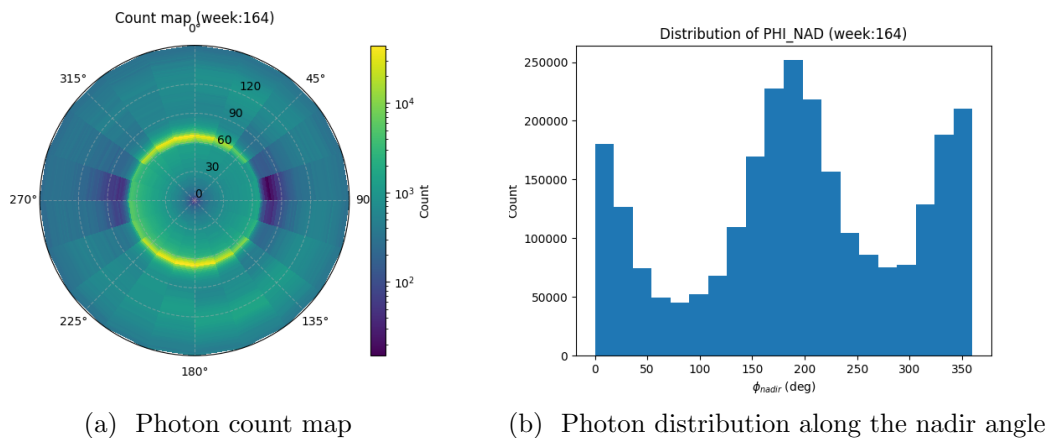


Figure 5.2: An example distribution of γ -ray from a single week

The limb's region could be easily observed in the bright ring above a dashed line of 60° nadir angle. Figure 5.2 an also shows the brightness of the

southern and northern hemispheres. Further investigating of the East-West effects could be illustrated by projecting the 2-D histogram into 1-D histogram of the nadir angle as in Figure 5.2b. Nevertheless, the explanation of the East-West a rough description and still incomplete since it does not take the exposure into account yet.

Applying criteria from the data selection such as event class, LAT's incident angle would affect the result from the histogram filling. In practice, each histogram was constructed for their belonging bin of the histogram in the energy domain. Hence, the multiple count map will be created for serving their energy ranges as in the Figure 5.3.

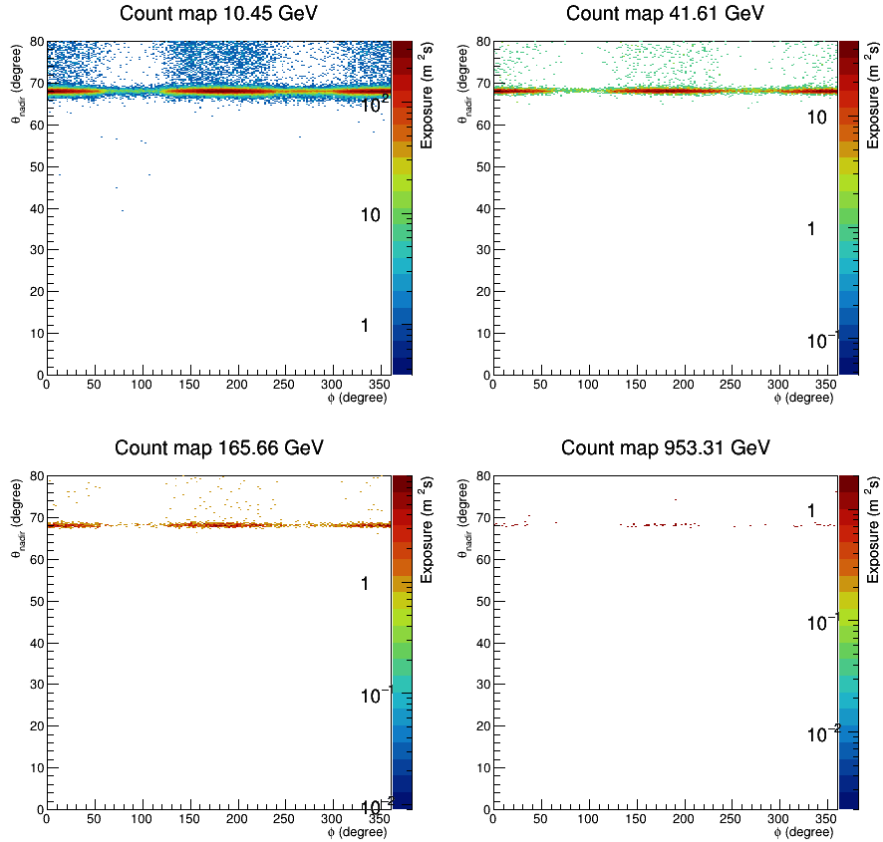


Figure 5.3: Cartesian plot of the photon histograms (title represent mean of the energy range)

However, looking at polar coordinate plotting from the cartesian point of view would not be a proper way. Figure 5.4 is another angle of viewing the same data but in their natural orientations. Both visualizations show that the Earth's

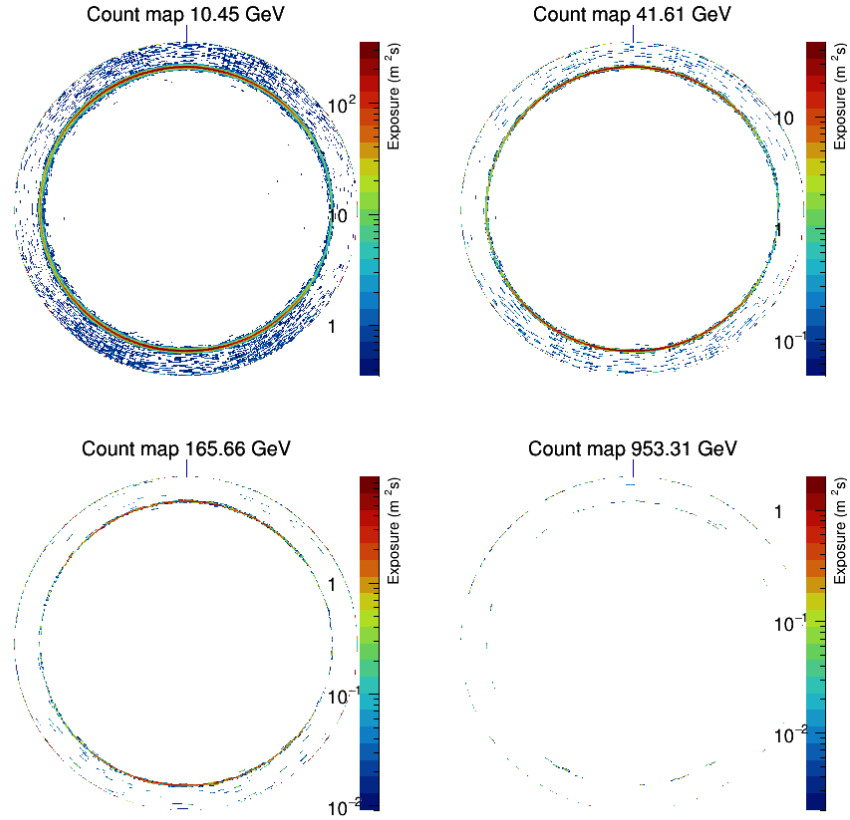


Figure 5.4: Polar plot of the photon histograms

limb region in γ -ray is the shiniest band for all interesting energy. It is also obvious to say that the more energy filtering condition, the less photon would match the criteria.

The next step is the exposure calculation. The exposure map is computed by accumulated exposure time from the LAT's FoV and also takes the effectiveness of the detector for correcting an angle dependency. By the end of the day, a unit from the calculation will be an area multiple by the time. The raw cartesian plot is visualized in Figure 5.5 with an attached axis.

The heatmaps show that the exposure intensity in the sky is much higher than the Earth in an order of magnitude because LAT was designed for seeking flare events in the space rather than looking at Earth. Regarding a given nadir angle between 60° to 70° , the spacecraft seems to look at the northern or southern hemisphere rather than the eastern and the western side. The color of

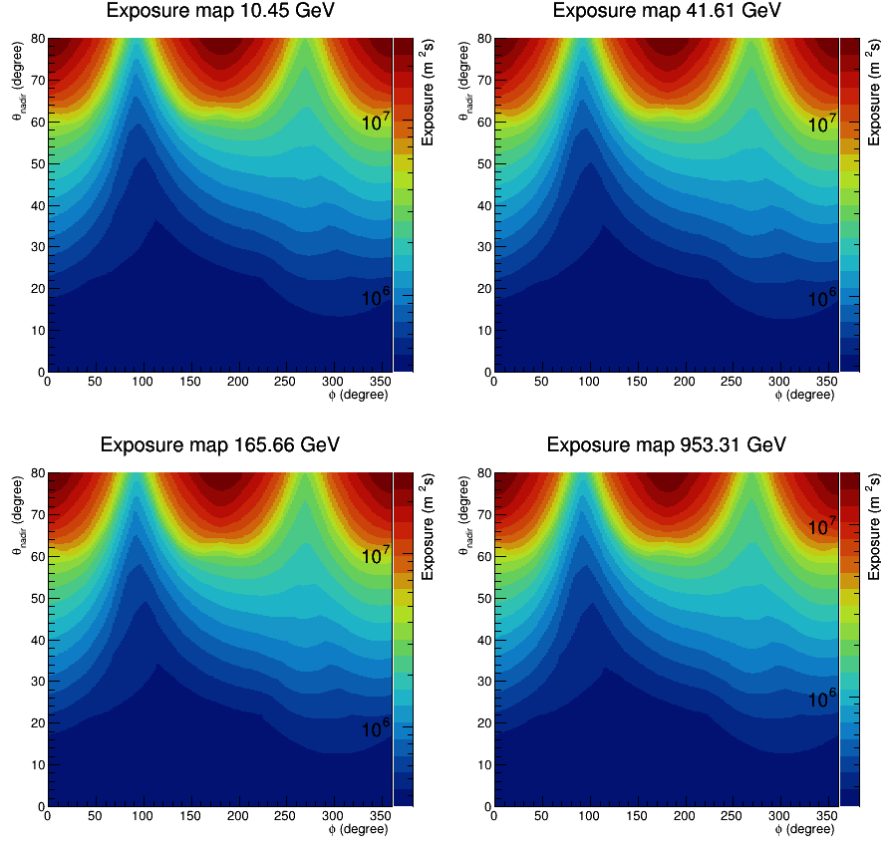


Figure 5.5: Cartesian plot of the exposure histograms

the at 270° (West) is more intense than 90° (East) means that the spacecraft tends to peek in the Westside more than Eastside. The reason might come from the trajectory of the charged particles were bent and produce a γ -ray which potentially could convince LAT to look at them rather than the other side because it has a chance to trigger the GBM. The 2-D histograms in polar coordinates have also been plotted in Figure 5.6.

The last step starts with initiating the new map that was defined by the division from the count maps and the exposure maps. After that, integrating the limb region in the polar coordinates to get a single scalar value. The scalar is then divided by the gap of the energy bin and the solid angle as a unitless quantity. Repeating a given description for all energy bins in the γ -ray spectrum and subtracts by the background would yield the final photon spectrum as in Figure 5.7.

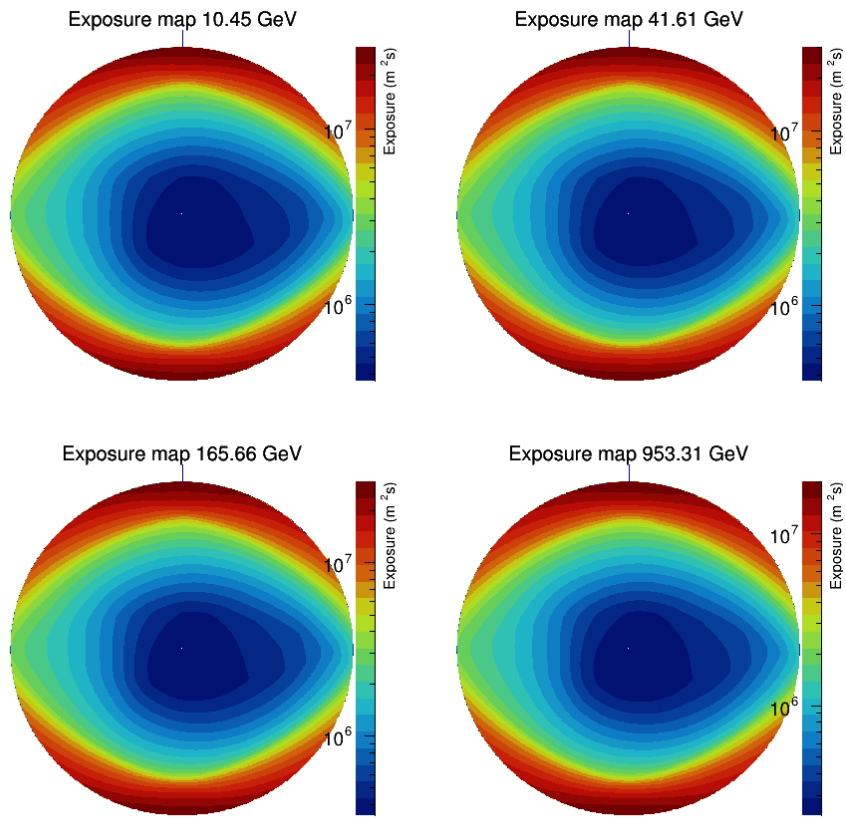


Figure 5.6: Polar plot of the exposure histograms

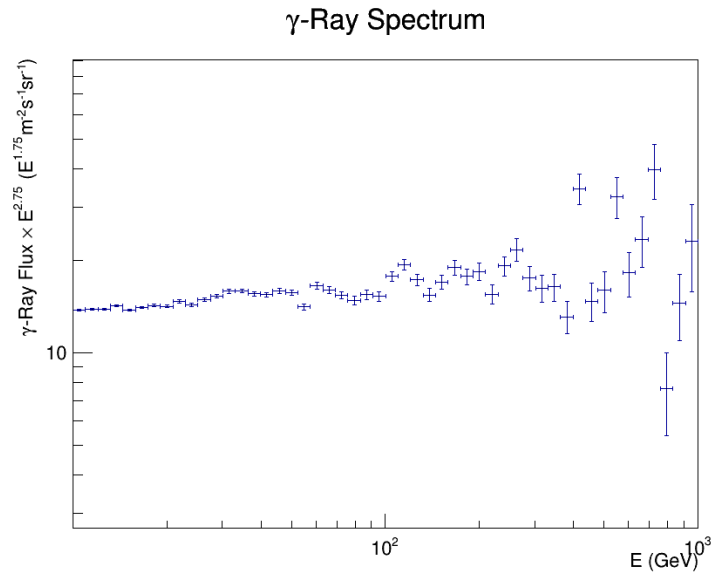


Figure 5.7: Measured γ-ray spectrum

In addition, exploring the γ -ray intensity from the visualization of the Earth's centered coordinates would be informative aspects to observe the variation of the photon intensity along the nadir angle as well as the East-West effect. The cartesian plotted is in Figure 5.8 and the polar form as in the Figure 5.9. Comparing the intensity along the peak of theta nadir in the cartesian plot from the East ($\phi=90^\circ$) and West ($\phi=270^\circ$) would reflect that the band of the intensity in the west is slightly thicker than in the East and the color of the peak center is more a little darker than the other side. It means that not only the intensity but also the ring thickness of the limb region is larger from West to East.

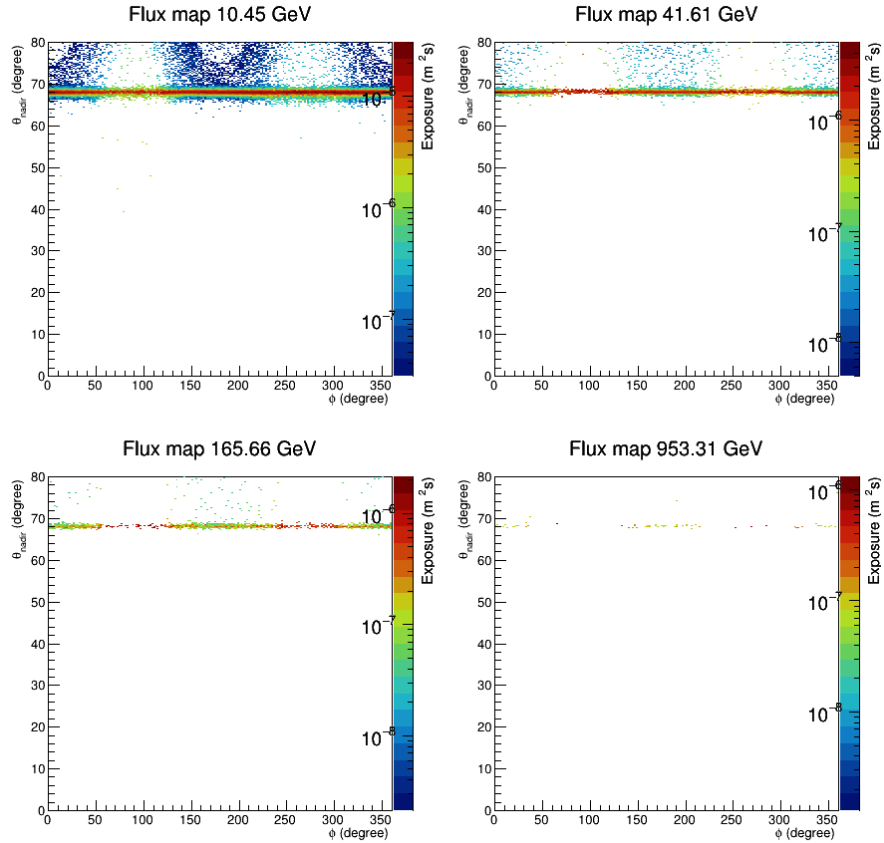


Figure 5.8: Cartesian plot of the flux histograms

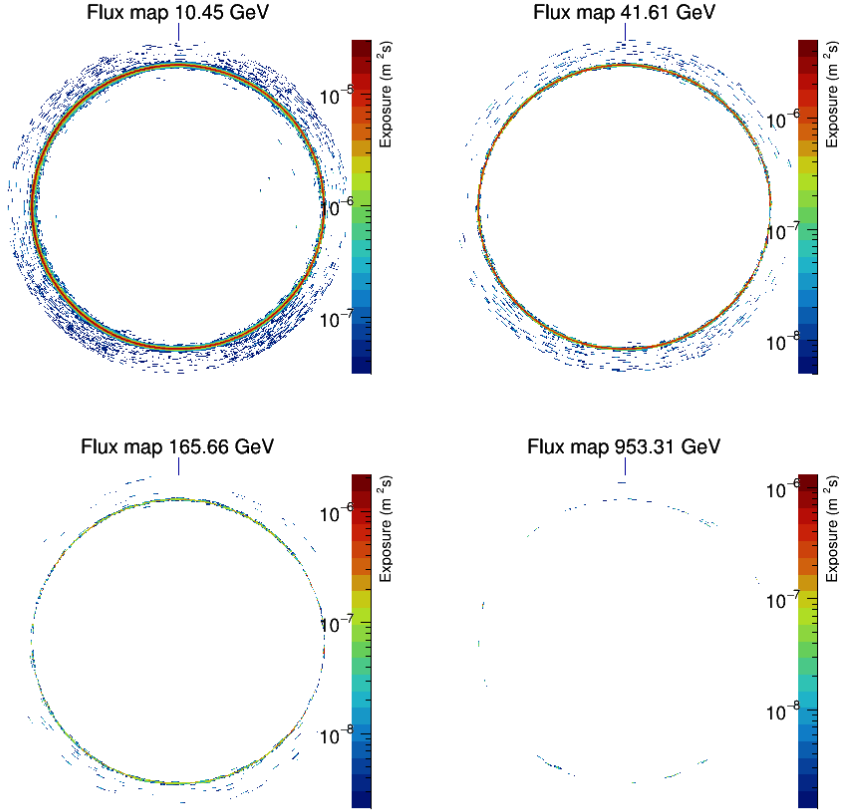


Figure 5.9: Polar plot of the flux histograms

5.3 Best fit result

The optimized parameters for SPL and BPL models are summarized in Table 5.1. Best fit γ -ray from both models are visualized in the Figure 5.10 along with spectrum from the measurement.

Best fits	γ_1	γ_2	E_{Break} (GeV)
SPL	2.70	-	-
BPL	2.86	2.63	333

Table 5.1: Optimization results

The comparative illustration also be visualized in the Figure 5.11 with a scaled spectra from both models to collate two other direct observations of the space-based experiments. It is obvious to see the consistency of BPL with the direct measurements in the bellowing sub-figure is more corresponding than the SPL model in the top sub-figure because the breaking point of the BPL does looks

more likely to be a proper model where the x-axis is the same rigidity scale.

However, a more complex model would perform better than the model that has less degree of freedom in practice. Determining the statistical significant would be the best way to answer whether CR spectrum is naturally described as a BPL indeed. The significant level could be determined by applying the objective function to Equation 4.17 for testing one-tail hypothesis-like from the null hypothesis comparing to an alternative hypothesis which is the model of breaking of spectral indices and non-breaking scheme or SPL versus BPL in another word. The significance is around 1.38σ or at 92%.

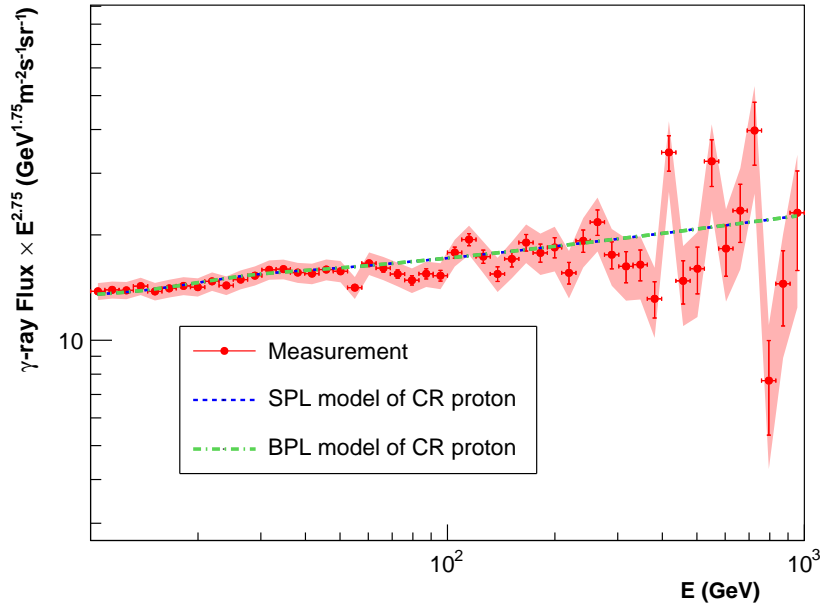


Figure 5.10: The γ -ray spectra calculated from the SPL (red) and BPL (blue) models of CR proton which best fit with the measured Earth's γ -ray spectrum in the thin-target regime (red)

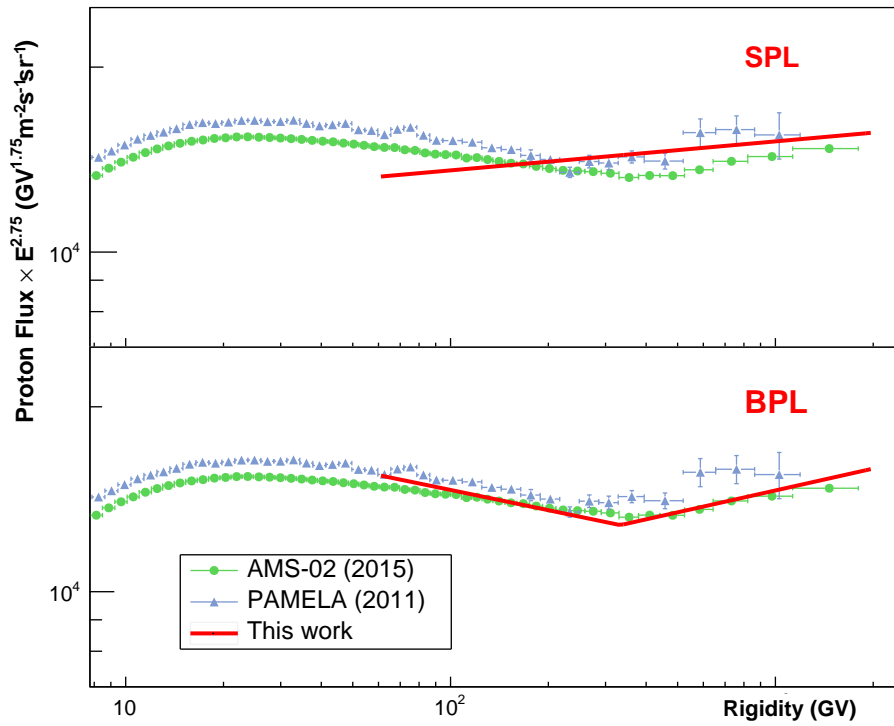


Figure 5.11: Best-fit CR proton spectrum from this work (red) compared to the measurements by AMS-02 (blue) and PAMELA (green)

CHAPTER VI

CONCLUSION

In this study, the incident CR proton spectrum was tracing by using the limb γ -ray. The measured γ -ray spectrum is constructing by taking the exposure of the LAT and the effective area into account where on the Earth-centered coordinates. The exposure calculation is calculated from the relation of the angle between the LAT's boresight and nadir angle because given nadir angle and the spacecraft orientation affects the performance of the measurement. After that, an indirect measurement of the proton spectrum was inversely computed via the $pp \rightarrow \gamma$ interaction model with a heuristic optimization technique.

Since the *Fermi*-LAT was launched in June 2008. The data has been collected from 7 August 2008 to 16 October 2017. The collection from 9 years of observations was recorded for both γ -rays data and the spacecraft orientation logging. The LAT mostly observing the sky and looking for a flare of γ -rays. However, there is a moment that LAT FoV can see the Earth or even stare at the Earth for some reason. Filtering photon from the Earth's limb region was done by selecting an incoming photon in the direction between $68.4^\circ - 70^\circ$ nadir angle with the cleanest event class.

To sum up, a statistical significance from the analysis yields 1.38σ . Meaning that there is a confidence level of breaking spectrum in CR proton at 92%. This level of significance is still now strong for confirmation. Nevertheless, the previous study with a few data collection periods gives 1.0σ significant level. It implicitly tells that the larger data collection could increase the statistics and put the weight on the previous study. Surprisingly, the direct CR proton measurement from AMS-02 identify a breaking spectrum at 340 GV which is very close to our work. There is also one plausible assumption where the indirect measurement could not yield a strong significant even we have a huge amount of data.

REFERENCES

1. Abdo, A. A., Ackermann, M., Ajello, M., Atwood, W. B., Baldini, L., Ballet, J., et al. (2009). Fermi large area telescope observations of the cosmic-ray induced γ -ray emission of the earth's atmosphere. *Phys. Rev. D*, 80, 122004.
2. Abdo, A. A., Ackermann, M., Ajello, M., Atwood, W. B., Baldini, L., Ballet, J., et al. (2009). Fermi large area telescope observations of the cosmic-ray induced γ -ray emission of the Earth's atmosphere. *Physical Review D*, 80(12), 122004.
3. Abraham, J., Abreu, P., Aglietta, M., Ahn, E., Allard, D., Allen, J., et al. (2010). Measurement of the energy spectrum of cosmic rays above 1018 ev using the pierre auger observatory. *Physics Letters B*, 685(4-5), 239–246.
4. Ackermann, M., Ajello, M., Albert, A., Allafort, A., Baldini, L., Barbiellini, G., et al. (2014). Inferred Cosmic-Ray Spectrum from Fermi Large Area Telescope γ -Ray Observations of Earth's Limb. *Physical Review Letters*, 112(15), 151103.
5. Ackermann, M., Ajello, M., Allafort, A., Atwood, W. B., Baldini, L., Barbiellini, G., et al. (2012). Measurement of Separate Cosmic-Ray Electron and Positron Spectra with the Fermi Large Area Telescope. *Physical Review Letters*, 108(1), 011103.
6. Adriani, O., Barbarino, G., Bazilevskaya, G., Bellotti, R., Boezio, M., Bogomolov, E., et al. (2009). An anomalous positron abundance in cosmic rays with energies 1.5–100 gev. *Nature*, 458(7238), 607–609.
7. Adriani, O., Barbarino, G., Bazilevskaya, G., Bellotti, R., Boezio, M., Bogomolov, E., et al. (2011). Pamela measurements of cosmic-ray proton and helium spectra. *Science*, 332(6025), 69–72.
8. Aguilar, M., Aisa, D., Alpat, B., Alvino, A., Ambrosi, G., Andeen, K., et al.

- (2015). Precision Measurement of the Helium Flux in Primary Cosmic Rays of Rigidities 1.9 GV to 3 TV with the Alpha Magnetic Spectrometer on the International Space Station. *Physical Review Letters*, 115(21), 211101.
9. Aguilar, M., Aisa, D., Alpat, B., Alvino, A., Ambrosi, G., Andeen, K., et al. (2015). Precision measurement of the helium flux in primary cosmic rays of rigidities 1.9 gv to 3 tv with the alpha magnetic spectrometer on the international space station. *Phys. Rev. Lett.*, 115, 211101.
 10. Aguilar, M., Aisa, D., Alpat, B., Alvino, A., Ambrosi, G., Andeen, K., et al. (2015). Precision Measurement of the Proton Flux in Primary Cosmic Rays from Rigidity 1 GV to 1.8 TV with the Alpha Magnetic Spectrometer on the International Space Station. *Physical Review Letters*, 114(17), 171103.
 11. Amsler, C., et al. (2008). Particle data group. *Phys. Lett. B*, 667(1).
 12. Atwater, T. W., & Freier, P. S. (1986a). Meson multiplicity versus energy in relativistic nucleus-nucleus collisions. *Phys. Rev. Lett.*, 56, 1350–1353.
 13. Atwater, T. W., & Freier, P. S. (1986b). Meson multiplicity versus energy in relativistic nucleus-nucleus collisions. *Physical review letters*, 56(13), 1350.
 14. Atwood, W., Albert, A., Baldini, L., Tinivella, M., Bregeon, J., Pesce-Rollins, M., et al. (2013). Pass 8: Toward the Full Realization of the Fermi-LAT Scientific Potential. *arXiv e-prints*, arXiv:1303.3514.
 15. Atwood, W. B., Abdo, A. A., Ackermann, M., Althouse, W., Anderson, B., Axelsson, M., et al. (2009). The Large Area Telescope on the Fermi Gamma-Ray Space Telescope Mission. *The Astrophysical Journal*, 697, 1071–1102.
 16. B., R., Ütikofer, E.O., F., & LÜCKIGER (2007). 30th international cosmic ray conference characteristics of near real-time cutoff calculations on a local and global scale.
 17. Baldini, L. (2014). Space-based cosmic-ray and gamma-ray detectors: a review. *arXiv preprint arXiv:1407.7631*.

18. Becquerel, H. (1896). On the rays emitted by phosphorescence. *Compt. Rend. Hebd. Seances Acad. Sci.*, 122(8), 420–421.
19. Belolaptikov, I., Budnev, N., Sinegovsky, S., Padusenko, A., Wiebusch, C., Moroz, A., et al. (1997). The baikal underwater neutrino telescope: Design, performance and first results. Tech. rep., SCAN-9704016.
20. Beringer, J., Arguin, J. F., Barnett, R. M., Copic, K., Dahl, O., Groom, D. E., et al. (2012). Review of particle physics. *Phys. Rev. D*, 86, 010001.
21. Bird, D., Corbato, S., Dai, H., Dawson, B., Elbert, J., Emerson, B., et al. (1994). The cosmic-ray energy spectrum observed by the fly's eye. *The Astrophysical Journal*, 424, 491–502.
22. Carlson, A., Hooper, J., & King, D. (1950). Lxiii. nuclear transmutations produced by cosmic-ray particles of great energy.-Part V. the neutral mesons. *Philosophical Magazine Series 7*, 41(318), 701–724.
23. Clay, J. (1927). Penetrating Radiation I. In Proceedings of the Royal Academy of Sciences Amsterdam. vol. 30, pp. 1115–1127.
24. Clay, J. (1928). Penetrating Radiation II. In Proceedings of the Royal Academy of Sciences Amsterdam. vol. 31, pp. 1091–1097.
25. Compton, A. H., & Turner, R. (1937). Cosmic rays on the pacific ocean. *Physical Review*, 52(8), 799.
26. Curie, M. (1923). Pierre Curie. Macmillan.
27. De Angelis, A. (2014). Atmospheric ionization and cosmic rays: studies and measurements before 1912. *Astroparticle Physics*, 53, 19–26.
28. Dembinski, H. P., Engel, R., Fedynitch, A., Gaisser, T., Riehn, F., & Stanev, T. (2017). Data-driven model of the cosmic-ray flux and mass composition from 10 GeV to 10^{11} GeV. In Proceedings of 35th International Cosmic Ray Conference — PoS(ICRC2017). Sissa Medialab.
29. Dermer, C. D., & Powale, G. (2013). Gamma rays from cosmic rays in supernova remnants. *Astronomy & Astrophysics*, 553, A34.
30. Dorman, L. (2009). First measurements of cosmic ray geomagnetic effects and the problem of CR nature. In Astrophysics and Space Science Library, Springer Netherlands. pp. 1–8.

31. Dorman, L. I., Fedchenko, S. G., Granitsky, L. V., & Rishe, G. A. (1970). Coupling and barometer coefficients for measurements of cosmic ray variations at altitudes of 260-400 mb. In International Cosmic Ray Conference. vol. 2, p. 233.
32. Ertley, C. (2014). Studying the polarization of hard x-ray solar flares with the gamma ray polarimeter experiment (grape).
33. Fermi, E. (1949). On the origin of the cosmic radiation. *Physical review*, 75(8), 1169.
34. Fricke, R. G., & Schlegel, K. (2017). Julius elster and hans geitel-dioscuri of physics and pioneer investigators in atmospheric electricity. *History of Geo-and Space Sciences*, 8(1), 1.
35. Gaisser, T. K., Stanev, T., & Tilav, S. (2013). Cosmic ray energy spectrum from measurements of air showers. *Frontiers of Physics*, 8(6), 748–758.
36. Gerward, L. (1999). Paul villard and his discovery of gamma rays. *Physics in perspective*, 1(4), 367–383.
37. Gray, G. W. (1949). Cosmic rays. *Scientific American*, 180(3), 28–39.
38. Greisen, K. (1966). End to the cosmic-ray spectrum? *Physical Review Letters*, 16(17), 748–750.
39. Haino, S., Sanuki, T., Abe, K., Anraku, K., Asaoka, Y., Fuke, H., et al. (2004). Measurements of primary and atmospheric cosmic-ray spectra with the bess-tev spectrometer. *Physics Letters B*, 594(1-2), 35–46.
40. Halzen, F., & Klein, S. R. (2010). Invited review article: Icecube: an instrument for neutrino astronomy. *Review of Scientific Instruments*, 81(8), 081101.
41. Hess, V. F. (1912). Über beobachtungen der durchdringenden strahlung bei sieben freiballonfahrten. *Phys. Z.*, 13, 1084–1091.
42. Huelsenbeck, J. P., & Crandall, K. A. (1997). Phylogeny estimation and hypothesis testing using maximum likelihood. *Annual Review of Ecology and Systematics*, 28(1), 437–466.
43. Hörandel, J. R. (2013). Early cosmic-ray work published in german. *AIP Conference Proceedings*, 1516(1), 52–60.
44. Isbert, J., Case, G., Granger, D., Guzik, T. G., Price, B., Stewart, M., et al.

- (2002). Atic, a Balloon Borne Calorimeter for Cosmic Ray Measurements. In CALORIMETRY IN PARTICLE PHYSICS. Proceedings of the Tenth International Conference. Held 25-29 March 2002 in Pasadena. pp. 89–94.
45. Kachelrieß, M., & Ostapchenko, S. (2012). Deriving the cosmic ray spectrum from gamma-ray observations. *Phys. Rev. D*, 86, 043004.
 46. Kelner, S. R., Aharonian, F. A., & Bugayov, V. V. (2006). Energy spectra of gamma rays, electrons, and neutrinos produced at proton-proton interactions in the very high energy regime. *Physical Review D*, 74(3), 034018.
 47. Kennedy, J., & Eberhart, R. (1995). Particle swarm optimization. In Proc. of ICNN'95 - Int. Conf. on Neural Networks. Perth, WA, Australia, vol. 4, p. 1942.
 48. Kirk, T. B., & Neddermeyer, S. H. (1968). Scattering of high-energy positive and negative muons on electrons. *Physical Review*, 171(5), 1412.
 49. Kolhörster, W. (1934). Cosmic rays under 600 metres of water. *Nature*, 133(3359), 419–419.
 50. Kraushaar, W., & Clark, G. (1962). Search for primary cosmic gamma rays with the satellite explorer xi. *Physical Review Letters*, 8(3), 106.
 51. Kraushaar, W., Clark, G., Garmire, G., Helmken, H., Higbie, P., & Agogino, M. (1965). Explorer xi experiment on cosmic gamma rays. *The Astrophysical Journal*, 141, 845.
 52. Kraushaar, W. L., Clark, G. W., Garmire, G. P., Borken, R., Higbie, P., Leong, V., & Thorsos, T. (1972). High-Energy Cosmic Gamma-Ray Observations from the OSO-3 Satellite. *The Astrophysical Journal*, 177, 341.
 53. Lesur, V. (2006). Introducing localized constraints in global geomagnetic field modelling. *Earth, planets and space*, 58(4), 477–483.
 54. Linsley, J. (1963). Evidence for a primary cosmic-ray particle with energy 10 20 ev. *Physical Review Letters*, 10(4), 146.
 55. Maldera, S. (2019). Fermi-lat performance,. https://www.slac.stanford.edu/exp/glast/groups/canda/lat_Performance.htm. Accessed:

2021-04-19.

56. Michelson, P. F., Atwood, W. B., & Ritz, S. (2010). Fermi gamma-ray space telescope: high-energy results from the first year. *Reports on Progress in Physics*, 73(7), 074901.
57. Millikan, R. A. (1932). Cosmic-ray ionization and electroscope-constants as a function of pressure. *Physical Review*, 39(3), 397.
58. Morris, D. J. (1984). Production of high-energy gamma rays by cosmic ray interactions in the atmosphere and lunar surface. *Journal of Geophysical Research*, 89, 10685–10696.
59. Morrison, P. (1958). On gamma-ray astronomy. *Il Nuovo Cimento (1955-1965)*, 7(6), 858–865.
60. Neddermeyer, S. H., & Anderson, C. D. (1937). Note on the nature of cosmic-ray particles. *Physical Review*, 51(10), 884.
61. Nuntiyakul, W., Evenson, P., Ruffolo, D., Sáiz, A., Bieber, J. W., Clem, J., et al. (2014). Latitude Survey Investigation of Galactic Cosmic Ray Solar Modulation during 1994-2007. *The Astrophysical Journal*, 795, 11.
62. Orth, C. D., & Buffington, A. (1976). Secondary cosmic-ray electrons and positrons from 1 to 100 gev in the upper atmosphere and interstellar space, and interpretation of a recent positron flux measurement. *The Astrophysical Journal*, 206, 312–332.
63. Petry, D. (2005). The Earth's Gamma-ray Albedo as observed by EGRET. In F. A. Aharonian, H. J. Völk, & D. Horns (Eds.), High Energy Gamma-Ray Astronomy. *American Institute of Physics Conference Series*, vol. 745, pp. 709–714.
64. Rochester, G., & Butler, C. (1953). The new unstable cosmic-ray particles. *Reports on Progress in Physics*, 16(1), 364.
65. Rossi, B. (1930). On the Magnetic Deflection of Cosmic Rays. *Physical Review*, 36, 606–606.
66. Rossi, B., & Greisen, K. (1941). Cosmic-ray theory. *Reviews of Modern Physics*, 13(4), 240.
67. Ruffolo, D., Sáiz, A., Mangeard, P.-S., Kamyan, N., Muangha, P., Nutaro, T.,

- et al. (2016). Monitoring Short-term Cosmic-ray Spectral Variations Using Neutron Monitor Time-delay Measurements. *The Astrophysical Journal*, 817, 38.
68. Seo, E., Ahn, H., Beatty, J., Coutu, S., Choi, M., DuVernois, M., et al. (2004). Cosmic-ray energetics and mass (cream) balloon project. *Advances in Space Research*, 33(10), 1777–1785. The Next Generation in Scientific Ballooning.
69. Shea, M., Smart, D., & McCracken, K. (1965). A study of vertical cutoff rigidities using sixth degree simulations of the geomagnetic field. *Journal of Geophysical Research*, 70(17), 4117–4130.
70. Sigl, G. (2012). High energy neutrinos and cosmic rays. *arXiv preprint arXiv:1202.0466*.
71. Skobeltzyn, D. (1929). The Angular Distribution of Compton Recoil Electrons. *Nature*, 123(3098), 411–412.
72. Skobeltzyn, D. V. (1985). The early stage of cosmic ray particle research. In Early History of Cosmic Ray Studies, Springer. pp. 47–52.
73. Stecker, F. W. (1973). Simple Model for Scanning-angle Distribution of Planetary Albedo Gamma-rays. *Nature Physical Science*, 242, 59–60.
74. Stephens, S. A., & Badhwar, G. D. (1981). Production spectrum of gamma rays in interstellar space through neutral pion decay. *Astrophysics and Space Science*, 76, 213–233.
75. Störmer, C. (1934). Critical remarks on a paper by g. lemaître and ms vallarta on cosmic radiation. *Physical Review*, 45(11), 835.
76. Svensson, G. (1958). The cosmic ray photon and π^0 -meson energy spectra at 29-30 km above sea-level. *Arkiv Fysik*, 13, 347.
77. Taylor, A. M. (2016). Cosmic rays beyond the knees. *Nature*, 531(7592), 43–44.
78. Thébault, E., Finlay, C. C., Beggan, C. D., Alken, P., Aubert, J., Barrois, O., et al. (2015). International geomagnetic reference field: the 12th generation. *Earth, Planets and Space*, 67(1), 79.
79. Thompson, D. J., Simpson, G. A., & Ozel, M. E. (1981). SAS 2 observations of the earth albedo gamma radiation above 35 MeV. *Journal of Geophysical*

- Research*, 86, 1265–1270.
80. Trenn, T. J. (1976). Rutherford on the alpha-beta-gamma classification of radioactive rays. *Isis*, 67(1), 61–75.
 81. Tsyganenko, N. A. (1987). Global quantitative models of the geomagnetic field in the cislunar magnetosphere for different disturbance levels. *Planetary and Space Science*, 35, 1347–1358.
 82. Van Allen, J. A., & Frank, L. A. (1959). Radiation around the earth to a radial distance of 107,400 km. *Nature*, 183(4659), 430–434.
 83. Van Oosterom, A., & Strackee, J. (1983). The solid angle of a plane triangle. *IEEE Transactions on Biomedical Engineering*, BME-30(2), 125–126.
 84. Wallace, J. M., & Hobbs, P. V. (2006). Atmospheric. Science.
 85. Watson, A. (2000). Ultra-high-energy cosmic rays: the experimental situation. *Physics Reports*, 333, 309–327.
 86. Wilks, S. S. (1938). The large-sample distribution of the likelihood ratio for testing composite hypotheses. *Ann. Math. Statist.*, 9(1), 60–62.
 87. Wilson, C. T. R. (1921). Iii. investigations on lighting discharges and on the electric field of thunderstorms. *Philosophical Transactions of the Royal Society of London. Series A, Containing Papers of a Mathematical or Physical Character*, 221(582-593), 73–115.
 88. Yoshida, S., Hayashida, N., Honda, K., Honda, M., Imaizumi, S., Inoue, N., et al. (1994). Lateral distribution of charged particles in giant air showers above 1 eev observed by agasa. *Journal of Physics G: Nuclear and Particle Physics*, 20(4), 651.

APPENDICES

APPENDIX A
TESTING THE EXPOSURE MAP

APPENDIX B

POWER LAW IN ENERGY

APPENDIX C

SUBTRACTING γ -RAY BACKGROUND

blabla

APPENDIX D
INTERACTION MODEL

BIOGRAPHY

NAME	Mr. Patomporn Payoungkhamdee
DATE OF BIRTH	29 April 1996
PLACE OF BIRTH	Bangkok, Thailand
INSTITUTIONS ATTENDED	Mahidol University, 2014–2017 Bachelor of Science (Physics) Mahidol University, 2018–2020 Master of Science (Physics)
HOME ADDRESS	86/46 Moo. 7, Bangmuang, Muang, Samutprakan 10270 Thailand
E-MAIL	patomporn.pay@student.mahidol.ac.th